Streamflow sensitivity to climate warming and a shift from snowfall to rainfall

By:

Katherine Hale

B.S., Georgetown University, 2014

A thesis submitted to the
Faculty of the Graduate School of the
University of Colorado in partial fulfillment
of the requirement for the degree of
Master of Arts
Department of Geography

2018

Thesis entitled:

Streamflow sensitivity to climate warming and a shift from snowfall to rainfall

Written by: Katherine Hale

has been approved for the Department of Geography

Dr. Noah Molotch

Dr. Suzanne Anderson

Dr. Andrew Badger

Date

The final copy of this thesis has been examined by the signatories, and we find that both the content and the form meet acceptable presentation standards of scholarly work in the above mentioned discipline.

Abstract

Hale, Katherine (M.A., Geography)

Streamflow sensitivity to climate warming and a shift from snowfall to rainfall

Thesis directed by Dr. Noah Molotch

As the climate warms, the fraction of precipitation falling as snow is expected to decrease. In snow-dominated mountainous regions, where reliance on snowpack and snowmelt is great, a reduction in snowfall fraction prompts us to examine downstream changes in streamflow and water resources. Shifts in precipitation phase are expected to alter the magnitude of ecosystem productivity, the timing of water resource availability, and, ultimately, the amount of annual streamflow. Here, I focus on the upper montane zone, which, in mid-latitude mountain ranges like the Rocky Mountains, is large and most vulnerable to changes in climate and warming. The objective of my study is to understand how climate warming, and associated shifts in evaporative demand, precipitation phase, and snowmelt timing will alter streamflow generation in the upper montane zone of the mid-latitude Rocky Mountains. The Distributed Hydrology Soil Vegetation Model is used to simulate streamflow within Gordon Gulch of the Boulder Creek Critical Zone Observatory, a watershed within the upper montane zone of the Colorado Front Range. I discover that streamflow decreases an average annual 37% under the influence of warming. But, on a seasonal time frame, streamflow increases in winter and spring months and decreases in summer and fall months. The presence of snow reveals a buffer-effect, decreasing the magnitude of streamflow loss compared to a snow-free environment. This buffering effect occurs because warming induces a shift in the timing of terrestrial water inputs from snowmelt and rainfall. In this context, terrestrial water inputs increase during a time of year when atmospheric water demand is relatively low, increasing the partitioning of terrestrial water inputs to streamflow. As a result, streamflow increases by 13% during winter and spring months, off-setting the net decrease in streamflow associated with warming. This off-setting effect has large implications for hydrological and ecological processes, and for water resource management across Earth's mountainous regions.

Acknowledgements

My advisor: Dr. Noah Molotch

My mentor: Dr. Adam Wlostowski

My committee members: Dr. Suzanne Anderson and Dr. Andrew Badger

The University of Colorado - Boulder Geography Department

The Institute of Arctic and Alpine Research

Boulder Creek Critical Zone Observatory

Nick Edwards for showing me how to do my own type of backflip

My family and friends for their unwavering support and enthusiasm

Longs Peak (Neníisótoyóú′u) for her demanding yet unassuming and inspiring presence

Contents

List of Tables

List of Figures

List of Abbreviations

CZO	**C**ritical **Z**one **O**bservatory
DHSVM	**D**istributed **H**hydrology **S**oil **V**egetation **M**odel
PET	**P**otential **E**vapo **T**ranspiration
SWE	**S**now **W**ater **E**quivalent
TWI	**T**errestrial **W**ater **I**nput

Chapter 1

Introduction

A warming climate is a catalyst for hydrologic change in the mountains. In the Western United States, the upper montane zone experiences an annual snow fraction of about 0.25-0.60 [Foster et al., 2016; Kormos et al., 2014]. Dependent on relative humidity and air temperature, snow falls when the temperature is roughly below 2.6C in the arid Rocky Mountains [Jennings et al., 2018]. A warming climate increases mean annual temperatures across the United States [Portmann et al., 2009], causing more precipitation to fall as rain instead of snow, decreasing the annual snow fraction [Kunkel et al., 2009; Mote et al., 2018]. The upper montane zone is particularly vulnerable to this change, as mean annual air temperature is above 0.0C and snowpack temperatures are typically around 0.0C [Klos et al., 2014; Marks et al., 1996]. Only small increases in temperature and energy are needed to force precipitation to fall as rain or to initiate melt [Marks et al., 1996]. Under warmer climate conditions, the total western U.S. is predicted to experience a decrease in area from 53% to 24% [Klos et al., 2014].

In the higher elevations of the Colorado Front Range, precipitation falls consistently as snow through the winter months, coinciding with snow water equivalent (SWE) accumulation. SWE, the amount of water contained within the snowpack, is highest at the end of the snow accumulation season [Sturm et al., 2010]. As spring air temperatures warm and precipitation shifts to rain, we see snow ablation and snowmelt [Marks et al., 1998; Barnett et al., 2005]. Together, the rain and snowmelt events generate terrestrial water input (TWI), the water supply to a catchment [Marks et al., 1998; Kormos et al., 2014]. Figure 1.1a portrays theoretical time-series of a present-day upper montane zone. Here, the storage of precipitation in the mountain snowpack acts to enhance the seasonality of TWI, where a relatively long winter dry period is followed by a relatively large pulse of TWI from snowmelt in the spring [Luce et al., 1998] Concurrently, potential evapotranspiration (PET), the potential rate at which a given climate will evaporate water from the soil-vegetation system, is low during winter months and high during summer months [Scheff and Frierson, 2014; Milly and Dunne, 2016]. Under this conceptualization of baseline TWI and PET phenology, time periods with low PET (i.e. low catchment water demand) coincide with low relatively low TWI (i.e. catchment water supply), and as PET increases in spring TWI also increases.

Under a warmer climate we expect air temperature to increase and snow fraction to decrease [Knowles et al., 2005]. SWE accumulation is shallower and less persistent and snow-covered area is reduced throughout the winter [Musselman et al., 2017; Kormos et al., 2014; Regonda and Rajagopalan 2004, Cayan et al 2001]. Snowfall shifts to rainfall earlier in the winter and spring, and snowmelt occurs intermittently during the winter and spring [Knowles et al., 2005; Musselman et al., 2017; Rasmussen et al., 2014; Barnhart et al., 2016]. The catchment no longer experiences one significant snowmelt event in the springtime, but instead intermittent melt events occur throughout the snow season. Figure 1.1b presents a theoretical conceptualization of the impacts of warming on snow fraction, TWI and PET in the upper montane zone. TWI echoes the intermittent patterns of winter melt and rain, changing the catchment TWI seasonality. The seasonal alignment between water supply to the terrestrial system (TWI as rainfall and snowmelt) and water demand (PET) is altered with unknown effects to catchment hydrology.

Additional environmental changes are expected to occur in a catchment under warmer conditions, as hydrology inherently connects the vegetative, soil and geologic systems in a catchment. I attempt to control such interactions throughout my study by using a hydrologic model to explore the impacts of warming on streamflow production.

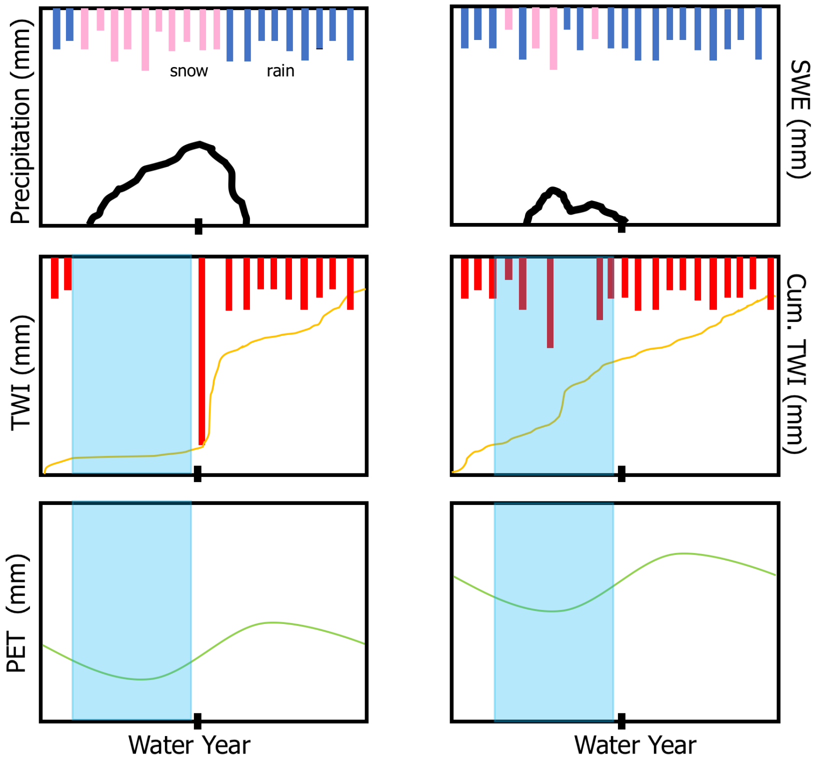

FIGURE 1.1: The theoretical hydrologic and evaporative trends across both a current and warmed upper montane catchment in one water year. Magnitudes (in mm) on the y-axis are relative to one another and the water year begins in October. The tick mark on the x-axis represents April 1. (a) In a present-day rain upper montane catchment, precipitation falls as snow throughout the winter, generating a greater annual snow fraction and resulting in a larger SWE accumulation. SWE increases into the spring until snowmelt begins. TWI coincides with rain and melt events, portraying a significant pulse during the snowmelt period. PET is low in the wintertime and high in the summertime. Highlighted in blue is the wintertime water supply (TWI as rainfall and snowmelt) and water demand (PET). Water supply is low when water demand is low. (b) In a warmer upper montane catchment, precipitation falls as both snow and rain throughout the winter, generating a lower annual snow fraction and resulting in a smaller SWE accumulation. Snowmelt occurs intermittently throughout the snow season, eliminating one large snowmelt pulse. TWI reflects this mixing of rain and melt events throughout the wintertime. PET is relatively higher, as the warmer air holds more water vapor. Here, highlighted in blue, water supply is high when water demand is low.

1.1 Hydrologic Modeling

Climate and streamflow predictions rely on hydrologic models to estimate future catchment conditions. The type of prediction relies on the selected hydrologic model and its capabilities. Broadly, hydrologic models can be classified as theoretical or empirical [Chow et al., 1988]. Theoretical models are physically-based, derived from physical laws and assumptions, whereas empirical models are derived from experimentation or observed input-output [Shaw, 1983; Chow et al., 1988; Cunderlick, 2003]. Empirical models can be further divided into stochastic and deterministic models [Jajarmizadeh et al., 2012]. Stochastic models are statistically based, applying probability equations to describe model parameters. Deterministic models have governing equations for every model under a given condition [Jajarmizadeh et al., 2012]. Types of deterministic models include lumped, semi-distributed and distributed models [Shaw, 1983; Cunderlick, 2003]. Spatial variability is assumed homogeneous in lumped models, whereas distributed models explicitly resolve spatial variability in model forcings and states throughout a catchment [Jajarmizadeh et al., 2012]. And while deterministic models require significant computational resources, they present a process-view of a catchment. A semi-distributed model overcomes the logistical requirements of a fully distributed model by using the observed average of many physical characteristics in a catchment to represent spatial heterogeneity [Gosain et al., 2009]. In this study, we wish to fully represent spatial variability within a catchment and therefore employ a fully distributed hydrologic model.

Impacts of climate warming on hydrology have been empirically investigated and modeled to show both decreases and increases in streamflow across a wide range of landscapes, elevations, and spatial/temporal scales [Gupta et al., 1998]. Historical trends in the nearby Upper Colorado River basin revealed 2% decreases in runoff efficiency, the amount of precipitation that becomes streamflow, for every 1^{o}C of warming [Nowak et al., 2012]. Goulden and Bales [2014] found that decreases in mountainous runoff occur due to increases in evapotranspiration in the Sierra Nevada, California. Bosson et al. [2012] saw similar trends in periglacial systems in Sweden. Luce et al. [2013] discovered decreases in streamflow in the U.S. Pacific Northwest were attributed to decreasing precipitation. Christensen et al., [2004] modeled the Colorado River Basin with the Variable Infiltration Capacity model, simulating "business-as-usual" climate warming and predicted streamflow decreases up to 17% by 2100. Both Milly et al. [2005] and Christensen and Lettenmaier [2007] used an ensemble of climate models to show a 10-30% decrease in runoff in the mid-latitude western North America by the year 2050 [Milly et al., 2005] and a 20% increase in the number of years with water shortages in the Colorado River Basin [Christensen and Lettenmaier, 2007]. Conversely, increases in regional precipitation revealed consistent empirical [Frans et al., 2013] and modeled [McCabe and Wolock, 2016] increases in streamflow generation. Streamflow change and magnitude differed geographically and temporally across the Colorado Rocky Mountains, greater United States, and internationally.

The majority of the aforementioned studies have focused on the effects of warming on annual streamflow. Fewer studies have identified the seasonal impacts of warming with regard to streamflow generation. One such study by Hamlet and Lettenmaier [1999] showed consistent increases in winter streamflow associated with increases in winter rain. As more rain events occurred in the wintertime months, water was immediately entering the catchment as direct precipitation as opposed to remaining stored within the snowpack until the snowmelt season [Hamlet and Lettenmaier, 1999]. Hamlet and Lettenmaier [1999] also simulated earlier snow melt, earlier spring peak streamflow, reduced runoff volumes and higher evapotranspiration in the summer months. Recent modeling efforts isolated mechanistic effects of warming on streamflow through coupled modeling [Foster et al., 2016]. Annually-based and event-based model simulations were run to identify streamflow responses to increased evapotranspiration and changes in precipitation phase [Foster et al., 2016]. Results showed that streamflow decreases are most influenced by increased evapotranspiration. These model results suggest that future increases in regional air temperature may have profound impacts on hydrological processes and water available and highlight TWI seasonality effects on streamflow [Kormos et al., 2014; Chauvin et al., 2011; Kapnick et al., 2018]. However, the impacts of changing TWI associated with warming have not been explored in detail. There remains a need to investigate water input seasonality influences on streamflow generation within mountainous domains [Foster et al., 2016; Berghuijs et al., 2014; Kapnick et al., 2018].

1.2 Budyko framework and hypotheses

I analyze output from my hydrologic modeling experiment through the Budyko framework, an empirical relationship relating catchment evaporative fraction to an index of its aridity Figure 1.2. Here, the catchment aridity index is defined as the ratio of potential evapotranspiration to precipitation (PET/P) and the evaporative fraction is defined as the ratio of actual evapotranspiration to precipitation (ET/P) [Budyko, 1974]. The Budyko framework is based on over 1200 long-term observations of the quantities noted from catchments around the globe [Budyko, 1974]. The framework can be used to predict the fraction of precipitation that will be partitioned to evaporation and streamflow (as a runoff ratio, 1-ET/P) based on a long-term average of aridity index. The Budyko framework assumes that catchment evapotranspiration (ET) is limited by energy in wet conditions (PET/P < 1) and by water in dry conditions (PET/P > 1) [Zhang et al., 2004]. Additionally, arid catchments (PET/P > 1) tend to evaporate a greater fraction of precipitation than humid catchments (ET/P < 1), but evaporative partitioning is more sensitive to changes in aridity within humid landscapes than arid landscapes [Budyko, 1974]. I relate these sensitivities to catchment hydrologic partitioning in the upper montane zone, assuming that changes in ET cause compensatory changes in streamflow (Q) [Berghuijs et al., 2014].

Anomalies from the predicted Budyko curve shed light on unexpected catchment behavior. Catchments experience over or underproduction of ET or Q if the evaporative fraction does not respond to the aridity as expected. These anomalies from the Budyko curve are associated with water and energy misalignment, where Q and ET are overproduced or underproduced in an environment [Barnhart et al., 2016]. For example, Figure 1.2 portrays a red point, the hypothetical aridity and evaporative indices of an upper montane catchment. If the catchment aridity index were to increase, like in a warmer climate, this point will move right on the x-axis. The Budyko framework predicts an expected change in the evaporative fraction, moving the point upwards on the y-axis. If the evaporative fraction changes as expected to a change in the aridity index, the behavior of the catchment will shift to the green point. However, if the evaporative fraction deviates from the expected curve, the catchment behavior may shift to the blue point. The blue point indicates a smaller change in the catchment evaporative fraction than the expected value. This underproduction in ET is analogous to an equivalent overproduction in Q, given that the runoff fraction (Q/P) is equivalent to 1 minus the evaporative fraction (i.e.

1-ET/P) [Budyko, 1974]. Previous work has used the Budyko framework and its relationship to Q, to show that watersheds with a lower snow fraction produce less annual streamflow than watersheds with a higher snow fraction [Berghuijs et al., 2014]. I look to further interrogate this result by determining the mechanism of hydrologic change. I ask: how does warming, and subsequent changes in timing of TWI and PET, affect annual streamflow generation within an upper montane catchment? I predict that a shift in TWI seasonality will decouple water supply and water demand and therefore produce relatively more streamflow in the winter and early spring months, alleviating the overall decrease in streamflow.

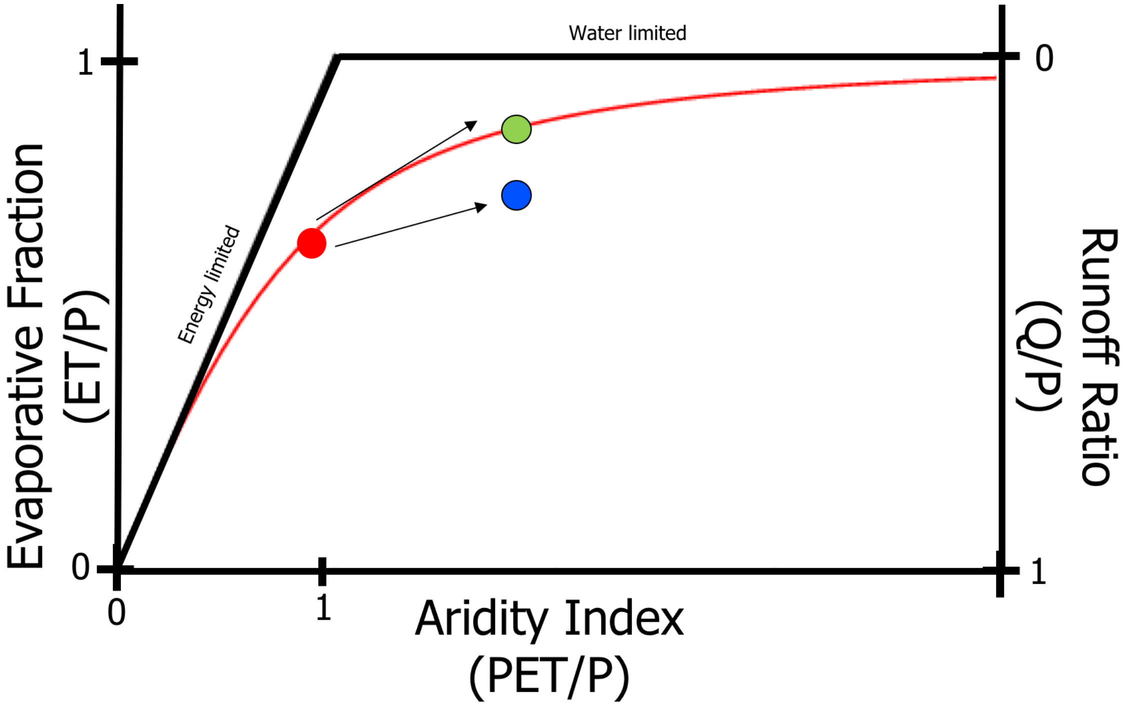

FIGURE 1.2: I place my research question within the framework of the Budyko curve [1974]. On the x-axis is the aridity index, the fraction of PET and P. On the y-axis is the evaporative fraction, the fraction of ET and P, and the runoff ratio, the fraction of Q and P (1-ET/P). The red line indicates Budyko's hypothesis of a regional relationship between aridity and evaporative indices. For every aridity index value, there is a corresponding and expected evaporative fraction. The red point symbolizes a present-day upper montane zone. The green point symbolizes expected movement along the Budyko curve due to warming. The blue point symbolizes reduced sensitivity, where an increase in PET leads to an increase in ET and a decrease in Q, but at a lower magnitude. Decreased sensitivity is attributed to a shift in TWI and a decoupling of water supply (TWI) and water demand (PET).

Chapter 2

Methods and Study Area

To simulate controlled and warming scenarios and to explore the mechanistic effects of warming, I use the Distributed Hydrology Soil Vegetation Model (DHSVM). I calibrate DHSVM to our study area by comparing model output to a variety of observations including: streamflow, snow depth, snow covered area, and soil moisture. I run a simulation with historical climate data over the period April 2010 – October 2013. This timeframe captures the longest streamflow record available, a high snow year and a significant monsoon season. The historically forced simulation represents my controlled scenario and the present-day upper montane zone with baseline conditions for snow fraction, SWE, TWI and PET. I next run a simulation based on a climate-warming scenario, representing the upper montane zone at the end of current century. This warming scenario reflects the total simulated change in snow fraction, SWE, TWI, PET, and the total hydrological impacts of climate warming in the upper montane zone. My analysis of warming influences includes a thorough annual and monthly comparison between the controlled and warmed simulation output, contrasting differences in PET, ET and Q. I use the Budyko curve to determine the specific influences of warming through due to changes in aridity index (PET/P), evaporative fraction (ET/P), and runoff ratio (Q/P). I assume that a change in

ET and Q in a simulated warmer climate is the sum of the effects of increased PET and changing precipitation phase linked to TWI seasonality. I subsequently analyze anomalies from the Budyko curve, assuming an anomaly is the effect of changing precipitation phase and TWI seasonality.

2.1 Distributed Hydrology Soil Vegetation Model

The Distributed Hydrology Soil Vegetation Model (DHSVM) is a spatially distributed numeric model, simulating the effects of topography, weather, soils, geology and vegetation on the hydrologic cycle [Wigmosta et al., 1994]. DHSVM is physically based, scalable to spatial and temporal resolution. Watershed energy balance and water balance are solved at each timestep. Set to user-defined input parameters, DHSVM serves as a predictive model to simulate future hydrologic conditions resulting from changes in land use or climate.

DHSVM has been applied across varying topography within North America to investigate climate, vegetation, disturbance and hydrology analyses at both the watershed and sub-watershed scales [Wigmosta and Lettenmaier, 1999; Yao and Yang, 2009; Westrick et al., 2002; Livneh et al., 2015; Raleigh et al., 2016]. Unlike the macroscale Variable Infiltration Capacity (VIC) model, its ability to capture high resolution, topographic complexity while perpetually solving for water and energy balance makes it the most suitable option for our modeling needs. I run DHSVM at a 20m resolution and at an hourly timestep.

DHSVM contains the following modules for calculating state and flux variables: an energy and mass balance model for snow accumulation and melt, a two-layer canopy model for evapotranspiration from vegetation overstory and understory, a two-layer rooting zone model and a saturated subsurface flow model [Wigmosta, 1994; Zhao et al., 2009]. The energy balance portion of the snow module calculates freeze, melt and heat content, whereas the mass balance portion calculates accumulation and ablation, snow water equivalent and water production [Wigmosta, 2001; Zhao et al., 2009]. Interaction between grid cells does occur, where water exchange and convergence occur as surface slope flow, route flow and soil moisture flow. Figure 2.1 portrays the flow of data, inputs and outputs required for and produced from DHSVM.

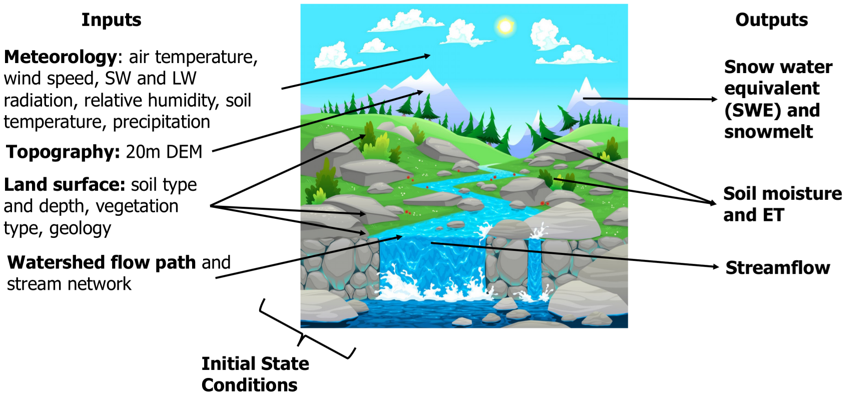

FIGURE 2.1: Input files required to run DHSVM to produce model output. Modules calculating state and flux variables for each timestep are not listed here.

2.2 Study Area: Gordon Gulch, Boulder, Colorado

Gordon Gulch of the Boulder Creek Critical Zone Observatory (BcCZO) outside of Boulder, Colorado is the ideal location to test our hypotheses within the semi-arid upper montane zone. Gordon Gulch (Figure 2.2) is located in the Colorado Front Range of the Rocky Mountains. The Gordon Gulch catchment includes an east-west oriented valley, carved by the east flowing Gordon Gulch stream, with north-south aspects. The catchment area is 2.6 km2 with an average elevation of 2500 meters and total relief of 291 meters [Diek et al., 2014]. Gordon Gulch is largely covered by evergreen forest. The north-facing slope consists of dense Lodgepole pines, and the south-facing slope consists of widely-spaced Ponderosa pines among grasses and shrubs [Diek et al., 2014]. Gordon Gulch experiences large seasonal temperature differences, with a yearly mean temperature of 5.1oC. Precipitation totals, on average, 520mm per year, with an average snow fraction of 0.60 [Cowie, 2010; Burns et al., 2016] and annual runoff ratios between 0.08-0.23 [Boulder Creek CZO, 2011]. The valley is underlain by 0.5-1.2 meters of soil, categorized as sandy loam, loamy sand and sand. Porosity of the soil ranges between 0.45 and 0.55 [Hinckley et al., 2012]. Below resides an intrusive igneous rock layer, consisting of granite, with gneiss outcroppings [Diek et al., 2014]. Depth to saprolite is between 30-35cm on the south facing slope and 40-45cm on the north facing slope [Diek et al., 2014; Hinckley et al., 2012; Befus et al, 2011].

One of most notable characteristics of the Gordon Gulch catchment is its prominent aspect control. Previous and ongoing investigations have credited aspect control as the underlying cause for differences in micro-topography, ecosystem dynamics, biogeochemistry, regolith thickness, soil composition, geologic weathering fronts, and melt season preferential flow paths [Hinckley et al., 2012; Langston et al., 2015; Anderson et al., 2011; Anderson et al., 2013; Gordon Gulch, 2011]. This known phenomenon allows for validation in natural differences between north and south facing hydrology.

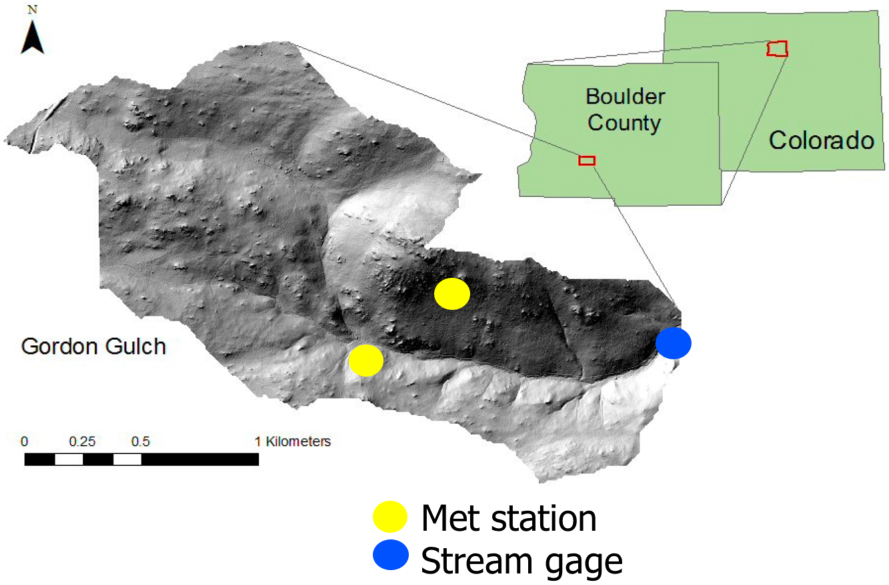

FIGURE 2.2: Gordon Gulch, the upper montane sub-catchment of the Boulder Creek CZO located just west of Boulder, CO. Gordon Gulch has two on-site meteorological stations and one streamflow gage. Surrounding the east-west flowing stream are prominent north and south facing aspects, differing in vegetation type and precipitation regime.

2.3 Data Inventory

2.3.1 Streamflow

Hourly and sub-hourly streamflow is reported in L/s from April 2010 to October 2013 [Zhang et al., 2018]. These data are determined from salt discharge injections ["Salt discharge measurement", 2016] and corresponding stage data. Discrete streamflow measurements are based off of Hongve [1987] and Kite [1993] due to low flows, where a known mass (M) of salt (NaCl) is mixed with water until dissolved and injected into the stream. Streamflow, Q, is then solved for using the following equation:

$$M = Q \int_{T}^{0} (C_{\mathrm{r}} - C_0) dt$$

M = mass of NaCl (in g)

Q = discharge in stream (m^3/s)

T = duration of the salt slug in the of stream water (long enough to see concentration or electrical conductivity of the stream rise to a peak, then fall back to baseline)

C_r = the concentration of NaCl in the river water

C_0 = the background concentration of salts in the river water

These discharge data have corresponding stage data. The stage and discharge data are used to create a rating curve for each water year. The rating curve is then used to convert subsequent stage measurements to discharge measurements throughout the year. This methodology inherently introduces uncertainty, as hydraulics in the stream channel can cause the salt injections to become trapped and discharge to appear higher than actuality. Channel sinuosity, vegetation, and the length of the chosen injection area affect stage readings as well. I account for streamflow uncertainty by bounding the observed time series by annual 95% confidence intervals [Surfleet et al. 2010; Kiang et al., 2018].

2.3.2 Meteorology

There are two meteorological stations within Gordon Gulch, one on the north and another on the south facing slope. Additionally, there is a National Atmospheric Deposition Program [NADP] station with a heated precipitation gage. The Gordon Gulch meteorological dataset spans from June 2012 to August 2018. I focus my work on water years 2011 through 2013, requiring data collection from nearby sources to gap-fill. Precipitation is reported as a combination of Sugarloaf NADP, Betasso met station, Gordon Gulch south facing met station and Niwot Ridge C1 met station data. I create a linear relationship between C1 and Sugarloaf NADP data and gap-fill Sugarloaf data with precipitation values informed by C1. Gap-filled Sugarloaf data are reported in the wintertime, from October to May. Gordon Gulch south facing precipitation data are reported in the summertime, from June to September, and gap-filled with Betasso met station data. I prioritize National Land Data Assimilation System (NLDAS) data due to erroneous time series in the Gordon Gulch met station data. But I inform NLDAS with Gordon Gulch station data when possible. NLDAS air temperature, wind speed, shortwave radiation, longwave radiation and relative humidity are used and bias corrected against Gordon Gulch and Betasso met station observations. I correct NLDAS air temperature with Gordon Gulch lower north facing met station air temperature data. I correct NLDAS wind speed and shortwave radiation with Gordon Gulch lower south facing met station data. I correct NLDAS relative humidity with Betasso met station data. NLDAS longwave radiation is considered sufficient for Gordon Gulch, given lack of additional observations. These data are reported on an hourly timestep.

My warming simulation is forced with 10-year average end-of-century climate anomalies generated by the Weather Research Forecasting (WRF) model [Gochis et al., 2013; Powers et al., 2017]. WRF output is an average of 19 global climate models, simulating "business as usual" warming. Based on historical data, WRF produces forecasting output based on geographic information at a 4km grid resolution [Powers et al., 2017; Gochis et al., 2013]. I combine change values from nine WRF output pixels. One pixel contains the Gordon Gulch sub-catchment and eight pixels surround Gordon Gulch. Each pixel represents a 10-year average of change values, and I take the average change value of the nine pixels. Change values for air temperature, relative humidity (derived from specific humidity) and longwave radiation have been added to the historical meteorological file to reflect warming. I hold precipitation constant in this experiment in order to isolate the hydrologic mechanism of changing TWI seasonality. I calculate change values by:

$$T_{\text{wrf}} = T_{\text{hist}} + \Delta T_{\text{wrf}}$$

Where, T_{wrf} is the predicted future air temperature, T_{hist} is the historic air temperature, and delta T_{wrf} is the change value between the 10-year average end-of-century WRF simulation and historic data. This equation is applied to relative humidity and longwave radiation as well (Figure 2.3).

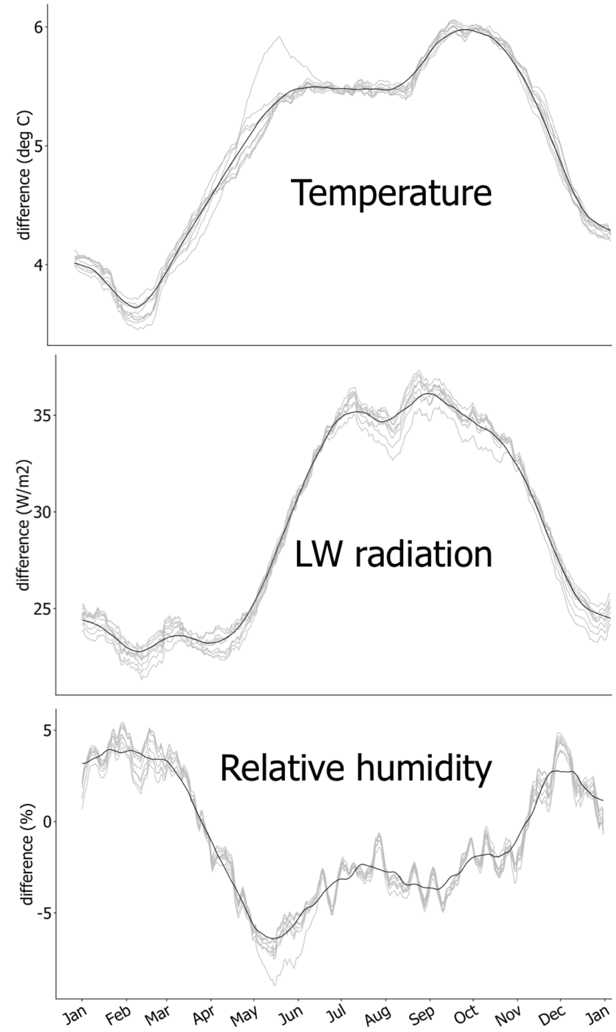

FIGURE 2.3: Air temperature, relative humidity and longwave radiation values generated from WRF end-of-century output. I gather change values from nine WRF pixels. One pixel includes the Gordon Gulch basin and eight pixels surround this central pixel. Time is on the x-axis and change values for each variable are on the y-axis. Each gray line represents a 10-year change average for one geographic pixel. The black line is an average of the 9 pixels. These change values have been added to the historical meteorological file to reflect warming.

2.3.3 Snow depth

Eight Judd ultrasonic snow depth sensors are located within the Gordon Gulch subcatchment, four on the lower north facing slope and four on the lower south facing slope. These sensors measure snow depth, relative to a snow-off depth measurement. Sub-hourly data, every 15-minutes, are available from April 2010 to October 2013, with gaps in time due to sensor malfunction. These data have been used to assist with determining soil water content, snow distribution and snow water melt paths in the upper montane zone [Hinckley et al., 2012; Langston et al., 2014; Williams et al., 2009]. I use these depth data to compare modeled SWE timing and snow-on and snow-off days. I overlay DHSVM SWE and average observed snow depth to look at trends between increasing and decreasing snow presence. One average depth time series is calculated for the sensors on the north facing slope and another time series is calculated for the sensors on the south facing slope. I am limited in comparing SWE and depth, as Gordon Gulch lacks consistent and spatially relevant snow pit density data to convert observed snow depth to SWE. Similarly, DHSVM does not calculate snow density to convert simulated SWE into snow depth. To objectively assess SWE and depth discrepancies, we calculate snow persistence, the percent of days with snow over the entire timeframe. I calculate an error of omission (number of simulated snow-off days where snow is observed) and an error of commission (number of simulated snow days where no snow is observed) to compare snow persistence between our simulation and the Gordon Gulch observations. Lastly, one snow pole course exists across upper Gordon Gulch, where snow depth is reported on weekly time steps [Williams et al., 2009]. I use these data for similar DHSVM SWE and observed depth temporal comparisons at a higher elevation.

2.3.4 Snow covered area

I use Landsat thematic mapper (TM) and ETM+ (Enhanced TM Plus) images to assess snow covered area (SCA) during April 2010-October 2013. ETM+ has a swath width of 185 km, with a typical photo covering an area of about 34,000 km2. The sensor system collects data in seven bands at resolutions of 30m for the visible, NIR and mid-infrared spectral regions [Gul et al., 2017; Huang et al., 2011]. The wavelength range is from 0.45 to 12.5m. After May 2003, there was a scan line problem with ETM+ images, limiting their use for image analysis [Gul et al., 2017]. Landsat imagery has been used to validate the accuracy of the MODIS daily snow products and Landsat registered DEM data in mountainous areas [Hall et al., 1995; Gul et al., 2017]. Most images were covered by clouds, especially during winter. Only cloud-free images were used for snow covered area analysis. A total of 21 Landsat images were downloaded for snow covered area observation. Six of these images have been used for higher detail analysis, one day from each winter month was selected to compare with spatially distributed DHSVM SWE maps.

2.3.5 Soil moisture

CS616 water content probes have been installed at various depths on lower Gordon Gulch north and south facing slopes [Hinckley et al., 2012]. Water content probes have been placed on the north facing slope and two on the south facing slope. Each probe has been installed to collect water content at roughly 5cm and 25cm into the ground surface at 10-minute intervals. The probes collect data as volumetric water content (VWC) [Hinckley et al., 2012; Diek et al., 2014]. Water content has been used to assess soil properties and aspect control of water movement within Gordon Gulch [Hinckley et al., 2012; Diek et al., 2014] and provide us with quality observed data for DHSVM comparison. I convert simulated percent soil saturation to volumetric water content by porosity, assigned as 0.46 for all three simulated soil layers [DHSVM, 2006; Hinckley et al., 2012]. I compare the average simulated VWC for soil depths of 10cm, 25cm and 40cm against the average observed soil VWC on the north and south facing slopes of Gordon Gulch.

2.3.6 Model input and output

A configuration file houses the path to several environmental input files, originating from regional and national datasets. My historical meteorological dataset, described above, forces long term climate and daily weather conditions within DHSVM. A 20-meter Digital-Elevation-Model (DEM) is derived from a 2010 1-meter LiDAR dataset encompassing the entire Boulder Creek CZO [Gordon Gulch, 2011]. This dataset is up-scaled to 20-meters, cropped to the Gordon Gulch sub-catchment and represents the topography of the catchment within DHSVM [Sharma et al., 2016]. The DEM provides the template for hillshade, soil depth, watershed boundary and stream network input files, which use topographic peaks and valleys to determine shading, depth and flow paths. Natural Resources Conservation Service (NRCS) provides soil type classifications at a 30-meter resolution [Natural Resources Conservation Service Soils, 2018]. These classifications are manually converted from the 18 NRCS soil classes to the predetermined 9 DHSVM soil codes. The U.S. Geological Survey has developed a similar database for geology across the U.S. The Colorado state geology shapefile has been reclassified to fit DHSVM specific geology codes [USGS, 2018]. PRISM climate data is a set of 30m gridded data products that informs DHSVM with spatial distribution patterns of meteorology [PRISM, 2018]. I input monthly PRISM maps to spatially distribute our forcing file within Gordon Gulch.

The input files combine to represent the makeup of Gordon Gulch within DHSVM. The output files represent the inner-workings of the catchment, including mass balance components, aggregated values and streamflow. For every timestep, DHSVM generates all energy and water balance variables and fluxes within the catchment. These output files are what we compare between control and warming simulations when I manipulate the input files to simulate a warmer climate.

2.3.7 Parameters

DHSVM includes physical parameters that are both fixed and unfixed in the defined watershed space. Parameters unfixed in space include soil and vegetation characteristics, which are defined differently across soil and vegetation type and depth to bedrock. Wigmosta et al. [2002] determined that roughly half of the unfixed model parameters are sensitive within hydrologic simulations. Yao and Yang [2009] focused on five of these parameters that most readily influence simulated evaporation, snow melt and run-off. Of these five, my simulations were initially sensitive to four parameters, listed in Table 2.1. Minimum resistance is the minimum stomatal resistance for passing water to the leaf sur- face for each vegetation layer (in s/m) [Wigmosta et al.,1994; Kaufmann, 1982; Alexander et al., 1985; Hunt et al.1991]. Greater minimum resistance suggests less water volume exiting the leaf and less water available for ET. Lateral conductivity is the rate of water movement through a saturated soil (in m/s) [Brooks and Boll, 2004]. The greater the lateral conductivity value, the greater the lateral water movement through the soil surface. Decreased lateral conductivity suggests little movement through the soil surface and more runoff above the surface [Brooks and Boll, 2004]. Exponential decrease is an exponent for change of soil conductivity at depth within a soil [Brooks and Boll, 2004].

A greater exponent indicates conductivity increases more rapidly with depth [Wigmosta et al., 1994]. Lastly, porosity is a measure of the void spaces in a soil, the fraction of the volume of voids to the total soil volume [Wigmosta et al., 2002]. The greater the soil porosity, the more water flows through the soil volume. These four parameters effect water availability on the vegetative or soil surface for ET or Q. Since I calibrate DHSVM to streamflow, correct water allocation is imperative to capture Gordon Gulch streamflow dynamics. From previous soil work in Gordon Gulch [Hinckley et al., 2012], vegetative explorations in shrub and forested areas [Antonarakis et al., 2010; Pope and Treitz, 2013; Brooks and Boll, 2004], and previous DHSVM calibration efforts [Wigmosta et al., 1994; Yao and Yang, 2009], I have selected baseline values for our four parameters of interest.

TABLE 2.1: Optimized DHSVM parameters for Gordon Gulch subcatchment.

Parameter	**Unit**	**Selected Value**	**Typical value ranges**
Minimum Resistance	s/m	0.280	200 – 800
Lateral Conductivity	m/s	0.001	10^{-5}˘10^{-2}
Exponential Decrease	m^{-1}	3.0	0 – 5
Porosity	m^3/m^3	0.46	0.46 – 0.6

2.3.8 Calibration

I first perform a local sensitivity test, changing model vegetation and soil parameters in a single, stepwise manner for the April 2010 to September 2013 timeframe [Du et al., 2014; Song et al., 2015]. I test sensitivity by running full simulations with parameter values ranging between 0.25 and 4 times the baseline value [Kuzmin et al., 2008]. I determine the optimal parameter value by calculating the Nash–Sutcliffe model efficiency co-efficient between (NSE) simulated and observed streamflow [Nash and Sutcliffe, 1970]. NSE is a normalized statistic that determines relative magnitude between simulated residual variance compared to observed variance, giving me a value between negative infinity and 1 [Krause et al., 2005; Nash and Sutcliffe, 1970]. The closer to 1 the NSE statistic, the more identical the variance values and better performing the model simulation. NSE is calculated using the following equation:

$$NSE = 1 - [\sum_{i=1}({Y^{\mathrm{i}}}_{\mathrm{obs}} - {Y^{\mathrm{i}}}_{\mathrm{sim}})^2 / \sum_{i=1}({Y^{\mathrm{i}}}_{\mathrm{obs}} - {Y^{\mathrm{i}}}_{\mathrm{mean}})^2]$$

Where ${\mathrm{Y}^{\mathrm{i}}}_{\mathrm{obs}}$ is the i^{th} observed streamflow value, ${\mathrm{Y}^{\mathrm{i}}}_{\mathrm{sim}}$ is the i^{th} simulated streamflow value, $\mathrm{Y}^{\mathrm{mean}}$ is the mean of observed data for streamflow and n is the total number of observations.

My stepwise sensitivity analysis allows me to narrow the range of parameter values. I next complete Latin hypercube sampling (LHS) with near-randomly selected parameter values [Muleta and Nicklow, 2005]. LHS, a type of stratified Monte Carlo sampling, selects n random values for each parameter within a given range [van Griensven et al., 2005; McKay et al., 1979; McKay, 1988; Manache and Melching, 2004]. I run 10,000 model simulations, each with a different combination of the four parameters, to further investigate parameter sensitivity and optimal parameter values [Du et al., 2014].

2.3.9 Limitations

The complexity of DHSVM inherently introduces uncertainty by exceeding the available data to force and validate the model. Fixed and unfixed parameters attempt to represent an intricate and dramatic landscape and capture environmental micro-dynamics and interactions. However, each parameter introduces an assumption about the landscape, where I often lack observed data [Stewart et al., 2017; Wigmosta, 1994; Du et al., 2014; Zhao et al., 2009]. This is particularly true with soil parameters, where porosity and field capacity are often known only to a range of values.

Chapter 3

Results

3.1 Model Performance

Of my four parameters of interest, lateral conductivity proves most sensitive within my step-wise model calibration simulations. The catchment becomes highly sensitive to water input as I incrementally increase and decrease lateral conductivity. Only slight increases in lateral conductivity create subdued responses in streamflow where the majority of the incoming water is absorbed into the soil. Alternatively, slight decreases in lateral conductivity create flashy responses, where incoming water immediately runs off the surface and does not enter the soil. I see this reflected in NSE values. In Figure 3.1,higher NSE values on the y-axis cluster toward the center of the x-axis. I further investigate this trend through Latin-hypercube sampling and narrow the parameter value range Figure 3.2. Here, I find that 0.001 (m/s) is the most optimal lateral conductivity value. Model simulations appear otherwise insensitive to the remaining parameters, suggesting large uncertainty within the forcing data (Figure 3.1).

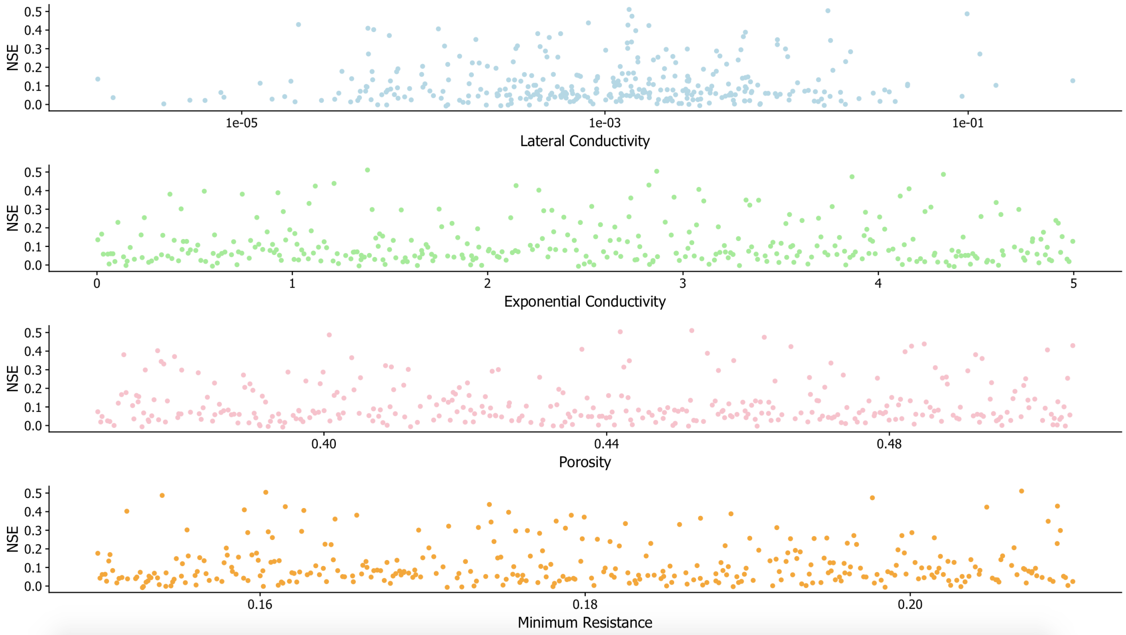

FIGURE 3.1: The results of my step-wise sensitivity test. NSE, on the y-axis, provides a metric for model performance: the higher the NSE value, the better the model performance and thus the more optimal the parameter value (x-axis). The combination of highest performing individual values results in the overall best performing version of DHSVM. Lateral conductivity is the only sensitive parameter I have tested.

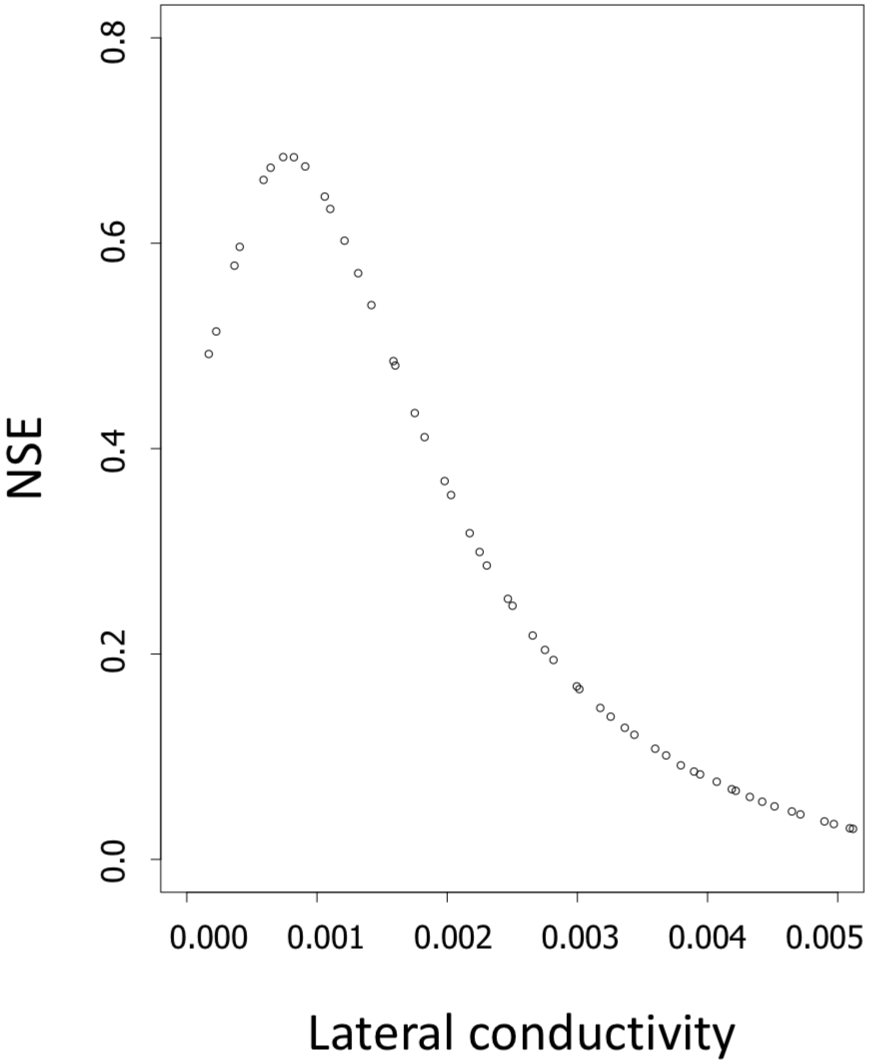

FIGURE 3.2: The results from narrowing the range of parameter values for lateral conductivity within Latin-hypercube sampling. I find that a lateral conductivity value of 0.001 creates the local the regional maximum NSE value.

After completing the calibration process, I move forward with a version of DHSVM that generates an NSE value, between observed and simulated streamflow, of 0.643. This statistic is consistent, if not higher, than previous work with DHSVM. Surfleet et al. [2010] used DHSVM for forest road and streamflow modeling in western Oregon, exceeding an NSE of 0.5 only 12% of the time. Van Wie et al. [2013] used the model for agricultural investigations in Washington and Idaho, obtaining NSE values of 0.5-0.69. Model performance was highest, 0.91, in watersheds where the model originated [Wigmosta and Burges, 1997] and was comparable to my output modeling work in surrounding mountainous regions, 0.57-0.88 [Beckers and Alila, 2004; Thyer et al., 2004). Surfleet et al. [2010] stated an NSE greater than 0.5 is acceptable for DHSVM calibration, to which I exceed and accept with known limitations.

These experimental limitations include previously mentioned forcing data uncertainty, methodology uncertainty, as well as a relatively short dataset for comparison (three water years) in an extremely small catchment with low streamflow [Surfleet et al., 2010]. Figure 3.3 shows the stage discharge data used to generate 95% confidence intervals around the observed streamflow data, where there is high uncertainty at both low and high observed flows (Figure 3.4) [Kiang et al., 2018]. Generally, DHSVM captures timing of Gordon Gulch peak flows but not magnitude. DHSVM simulates lower peak flows than observed. Additionally, the model simulates rising peak streamflow earlier than observed and falling peak streamflow later than observed. Flashy rain events, those that generate high and immediate runoff, are captured in both observed and simulated data. Overall, DHSVM generates more streamflow than is observed, despite missing peak flow height. Observed runoff ratio is 0.16, simulated is 0.32. Much of the overestimation is captured through observed streamflow uncertainty, where runoff ratios range from 0.11-0.23. I seek non-numerical validation and ensure that, despite streamflow uncertainty, the model captures topographic controls between the north and south aspects.

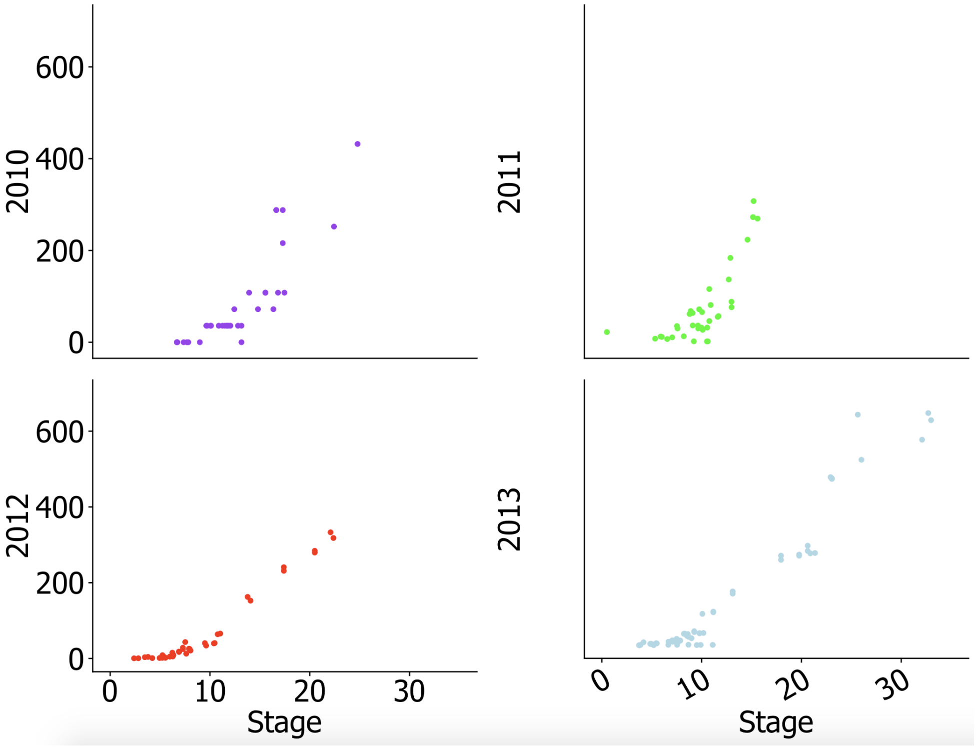

FIGURE 3.3: Annual relationships between Gordon Gulch stage, the height of water, on the x-axis and discharge, the rate of streamflow, on the y-axis. Generally, as stage increases, discharge increases, portraying a positive relationship. The scatter among these data suggest uncertainty, to which I quantify as annual 95% confidence intervals in Figure 3.4.

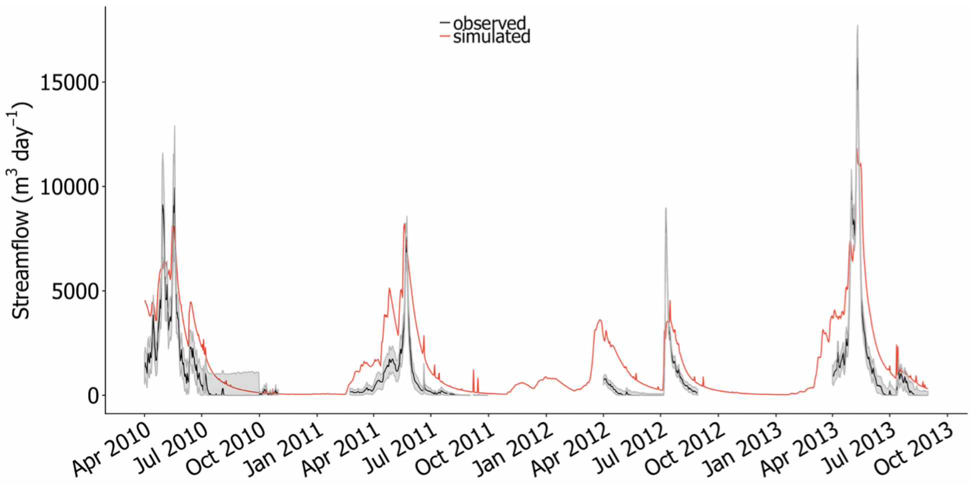

FIGURE 3.4: A streamflow time series with time on the x-axis and streamflow (in m3/day) on the y-axis. Observed Gordon Gulch streamflow (black) bounded by 95% confidence intervals (gray) and DHSVM simulated streamflow (red). The NSE value comparing bounded observed streamflow and simulated streamflow is 0.643. The observed runoff ratio is 0.16, with an uncertainty range from 0.11 to 0.23. The simulated runoff ratio is 0.32.

3.1.1 SWE and SCA

It is known that SWE and SCA differ across the north and south facing aspects of Gordon Gulch [Hinckley et al., 2012; Williams et al., 2009; Anderson et al., 2011; Anderson et al., 2013]. Figure 3.5 shows differences in simulated SWE and observed depth between the north and south facing slope. Greater SWE and depth persist on the north facing slope than the south facing slope. Both slopes show similar trends in snow presence between observed and simulated data. For example, on the south facing slope a snow event occurs in February 2011 where both SWE and depth increase quickly, persist for a few days and decrease at a slower rate. The same trends occur during snow events in November and December 2011. On the north facing slope, snow trends align between simulated SWE and observed depth during a February 2011 snow event and throughout the 2012 snow season (November 2011 to April 2012). The same trends occur during snow events in November and December 2011. On the north facing slope, snow trends align between simulated SWE and observed depth during a February 2011 snow event and throughout the 2012 snow season (November 2011 to April 2012).

Similarly, snow persistence is greater on the north facing slope than the south facing slope in both the simulated and observed data. Snow persistence is greater within observed data on both the south and north facing slopes than simulated data. South facing simulated snow persistence is 21% , observed is 33% . North facing simulated snow persistence is 36%, observed is 58%. Our south facing error of omission is 16% of all snow days and error of commission for 10% of all non-snow-cover days. Our north facing error of omission is 25% of all snow days and error of commission is 4% of non-snow-cover days. Collectively, these data reveal that simulated SWE trends follow those of observed snow depth in timing and magnitude. Consistent discrepancies appear as the model underestimates snow presence. While I do not calculate snow persistence for discrete snow pole data, we do see similar temporal alignment between north and south facing snow pole observations and DHSVM output at this location (Figure 3.6).

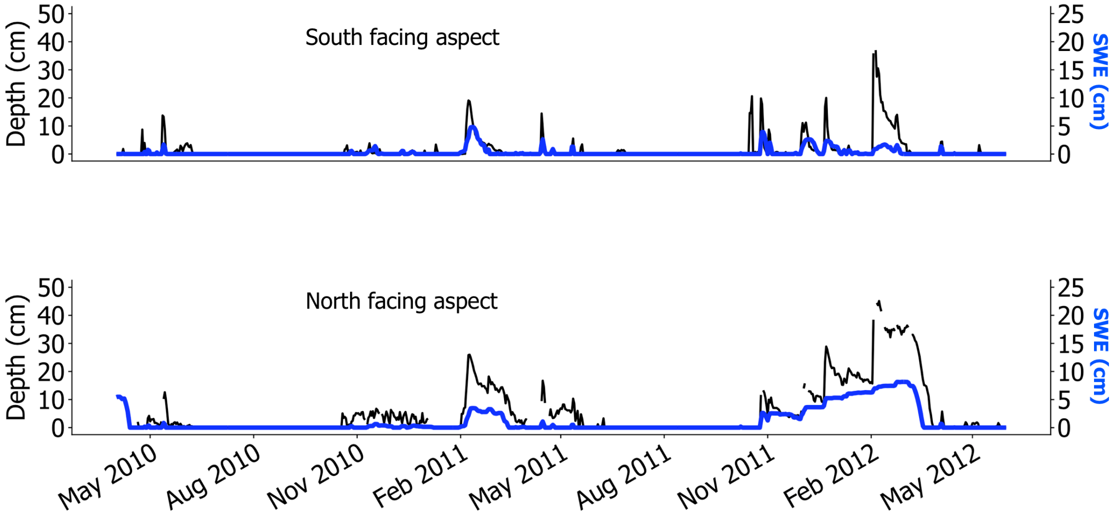

FIGURE 3.5: A time series of observed snow depth and modeled SWE in Gordon Gulch. Average snow depth sensor observations (black) are overlaid with simulated SWE output (blue) on both south and north facing slopes of Gordon Gulch. The x-axis of each plot is time (April 2010 to October 2013) and the two y-axes represent depth in cm (snow depth on the left, SWE depth on the right). Snow presence, accumulation and melt trends appear similar between both datasets. With insufficient observed or simulated snow density data, I compare only temporal patterns here. The north facing slope, in both simulated and observed data, has more snow accumulation than the south facing slope. Generally, a snowpack persists on this slope, versus intermittent accumulation and ablation on the south facing slope. On the south facing slope, we see similar increases and decreases in snow depth and SWE during snow events in February 2011 and November and December 2011 into February 2012. Similarly, we see corresponding increases and decreases in snow between simulated SWE and observed depth on the north facing slope during February to April of 2011 and the entire 2012 snow season.

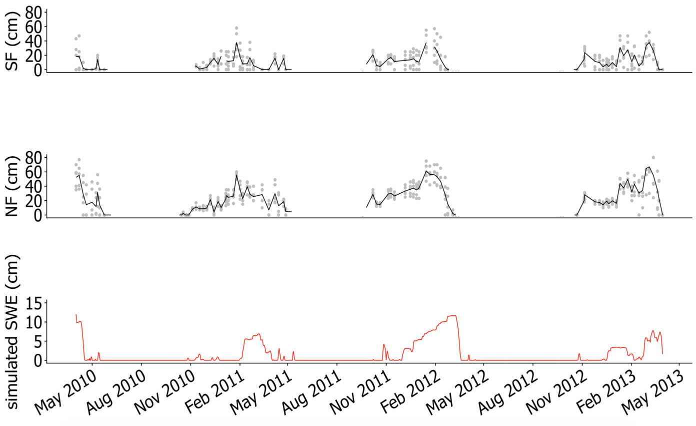

FIGURE 3.6: Observed south and north facing snow depth and DHSVM simulated SWE at Gordon Gulch upper snow pole site. The x-axis represents time and the y-axes represent depth (upper two panels) and SWE (bottom panel) in cm. Within observed depth measurements, points represent the discrete depth measurements and the line represents average depth. This site is higher in elevation than the previous snow depth sensors. Consequently, we see slightly higher observed depths and simulated SWE values here than on the lower north and south facing slopes. The 2012 snow season in particular, November 2012 to May 2012, temporally aligns in accumulation and ablation with the north facing snow pole measurements. Despite very discrete depth observations limiting our temporal comparison, we see general alignment in timing and magnitude within the simulated SWE.

Figure 3.7 shows discrete Landsat7 TM and ETM+ SCA observations and simulated SWE distribution maps from winter months during our timeframe of interest. The SCA and SWE data reveal greater snow accumulation in the upper portion of Gordon Gulch. This can be seen across the first three winter dates. Modeled SWE shows obvious contrasts between north and south facing slopes of Gordon Gulch that are also seen in observed SCA on March 20, 2013. Generally, the comparisons between Landsat and DHSVM output are difficult to make, though some qualitative similarities in the spatial patterns indicate that the model is capturing portions of the snow spatial variability in Gordon Gulch.

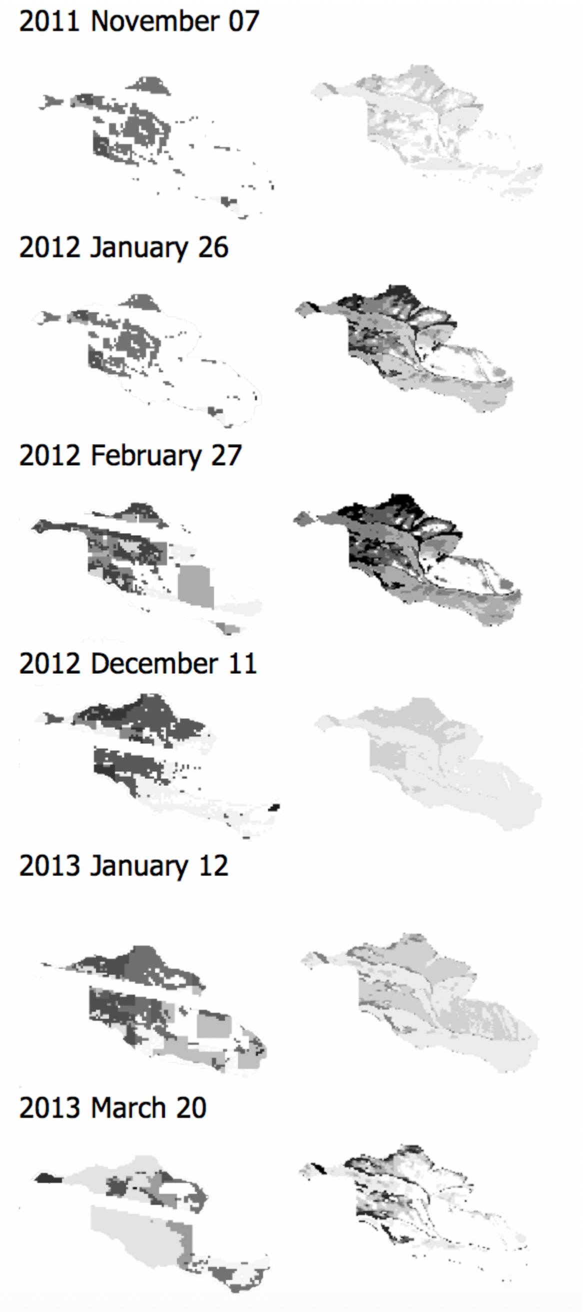

2011 November 07

2012 January 26

2012 February 27

2012 December 11

2013 January 12

2013 March 20

FIGURE 3.7: Landsat SCA imagery (left column) and DHSVM SWE output (right column) for coinciding winter dates. Each image is a discrete observation. Darker shading indicates greater SCA or SWE. Error lines exist in LandSat7 data. While comparisons are limited to qualitative assessments, we see trends in snow on and off, especially between the upper portion of Gordon Gulch and the lower portion.

3.1.2 Soil moisture

I assess soil moisture as my next form of model validation. Figure 3.8 shows soil moisture at three simulated soil depths with the average observed soil moisture of four soil plots across Gordon Gulch. Observations and model estimates of volumetric water content (VWC) on north and south facing aspects exhibited significant similarity. Across both aspects of Gordon Gulch, simulated VWC increases earlier in the winter to spring seasons compared to the observed VWC, particularly at 10cm and 25cm. The 40cm simulated soil layer appears to emulate deeper base flow. At this depth, seasonal increases occur far later than observed soil layers. However, the magnitudes of VWC across observed and simulated soils are similarly very dry, with VWC values below 0.2, throughout the year [Hinckley et al., 2012].

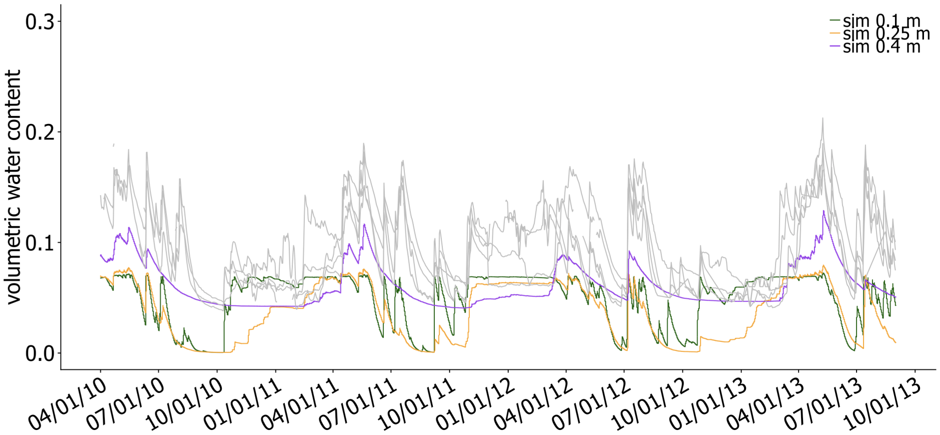

FIGURE 3.8: Average volumetric water content between three simulated soil layers (colored lines) and various depths across four soil plots within Gordon Gulch. Magnitude of VWC and dryness are similar between simulated and observed soils, though timing of moisture peaks differs seasonally.

3.2 Control and WRF simulations

The first step in investigating streamflow response to warming through DHSVM is to evaluate the differences between the control and warming simulations. Figure 3.9 portrays a time series of modeled SWE, TWI, cumulative TWI, and PET for the control and warming scenarios. In the control simulation Figure 3.9a, the snow fraction is 0.36 with a prominent SWE accumulation every snow season. Maximum SWE is 49mm in 2011, 81mm in 2012 and 53mm in 2013. TWI seasonality reflects direct precipitation events and snowmelt. PET also reflects seasonality and is low during the wintertime and high during the summertime. PET averages 647mm per year. The warming simulation, Figure 3.9b, reflects a decreased snow fraction of 0.31 with significantly decreased SWE accumulation. Maximum SWE is 42mm in 2011, 22mm in 2012, and 31mm in 2013. TWI seasonality and PET seasonality are still present. PET averages 955mm per year.

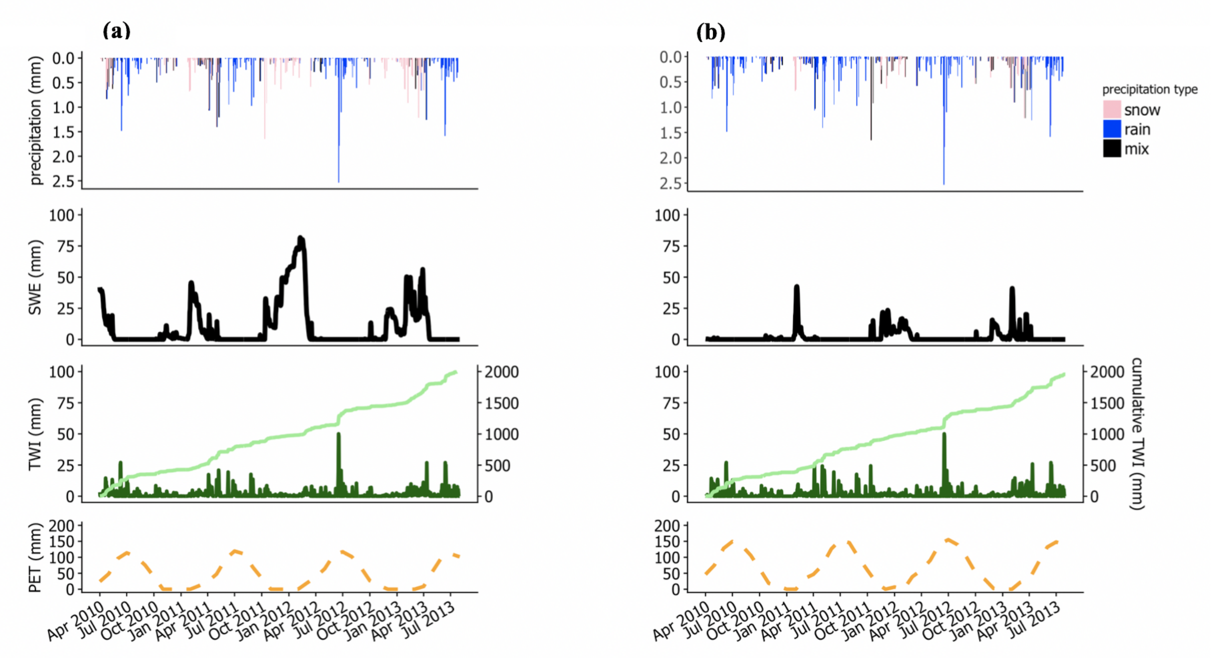

FIGURE 3.9: The DHSVM hydrologic output from the controlled and warming simulations. On the x-axis is time and on the y-axes are mm of precipitation, SWE, TWI, cumulative TWI and PET. (a) reflects the controlled simulation. Incoming precipitation reflects a snow fraction of 0.36 over the entire time period. SWE accumulation is prominent over every snow season. TWI reflects rainfall and melt events and cumulative TWI is a sum of all TWI over the time period. PET reflects seasonality, with the higher PET values in the summertime. In our control simulation, high water supply (TWI as rainfall and snowmelt) corresponds with high water demand (PET) in late spring and summer months. Conversely, (b). reflects the warming simulation. Under warmer conditions, there is a reduced snow fraction of 0.31. SWE accumulation is less prominent than the controlled simulation. TWI still reflects the rainfall and snowmelt events, but these events are shifted toward earlier in the water year. PET remains seasonal. In the warming simulation, high water supply (TWI as rainfall and snowmelt) now occurs more evenly throughout the year and is no longer aligned with high water demand (PET).

Total TWI in control and warming scenarios were the same, yet TWI seasonality changes as shown in Figure 3.10. A shift in TWI seasonality is apparent in the warming scenario with increased TWI in winter and spring months; more rain and melt events occur earlier in the water year. This is also a time of relatively low PET. In the spring and summer, the control simulation experiences a large input of TWI from snowmelt and TWI increases more rapidly than the warming simulation. The timing of this spring TWI pulse is also a time of year with relatively high PET. This temporal shift in TWI between control and warming scenarios occurs across all three water years.

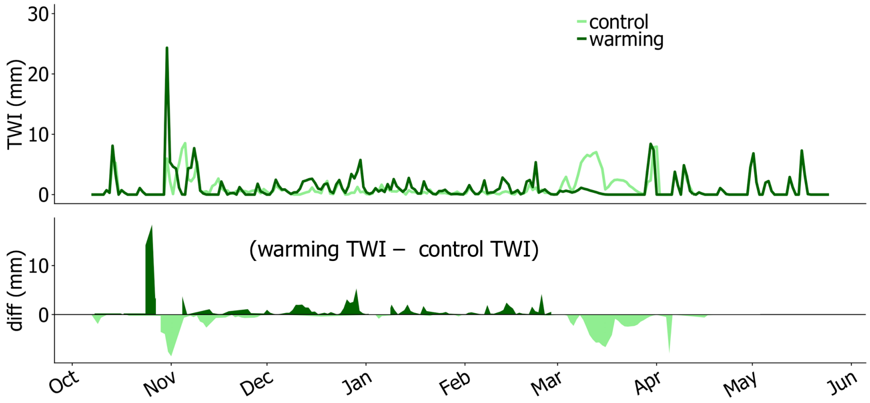

FIGURE 3.10: The top panel portrays daily TWI in the controlled (light green) and warming simulations (dark green). TWI is greater in the warming simulation during winter and spring months. The increase coincides with greater rain and melt events occurring in the wintertime. Conversely, TWI is much greater in the control simulation during late spring, when a large snowmelt event occurs. The bottom panel shows this difference in TWI by subtracting control TWI from warming TWI. When TWI difference is positive (dark green), warming TWI is greater than control TWI. When the TWI difference is negative (light green), control TWI is greater than warming TWI. Similarly to the top panel, areas of positive difference are concentrated in the winter months and areas of negative difference are concentrated in the late spring months.

Figure 3.11 reflects the monthly differences in the water balance between the control and warming scenarios. During all months, the difference between warming and control PET is a positive value, revealing a continual increase in PET under warmer conditions. During most months, the difference between warming and control ET is also positive, with exceptions in June 2010, July 2010, August 2010, June 2011, July 2011, August 2011, May 2012, June 2012, August 2012, June 2013, and August 2013. These months, primarily summer months, reveal decreases in ET in the warming simulation. During most months, the difference between warming and control Q is negative, reflecting an overall decrease in streamflow. Exceptions to this behavior occurred in February 2011, March 2012, February 2012, January 2012, and March 2013. These months, primarily winter and spring months, reveal increases in Q in the warming simulation. On an annual average, the warming simulation decreases Q by 31mm, 37% of total annual runoff. However, annual increases in Q average 11mm, 13% of total annual runoff. Monthly increases in Q, under warming conditions, were associated with increased seasonal TWI, water supply, during winter months when evaporative demand (i.e. PET) was relatively low.

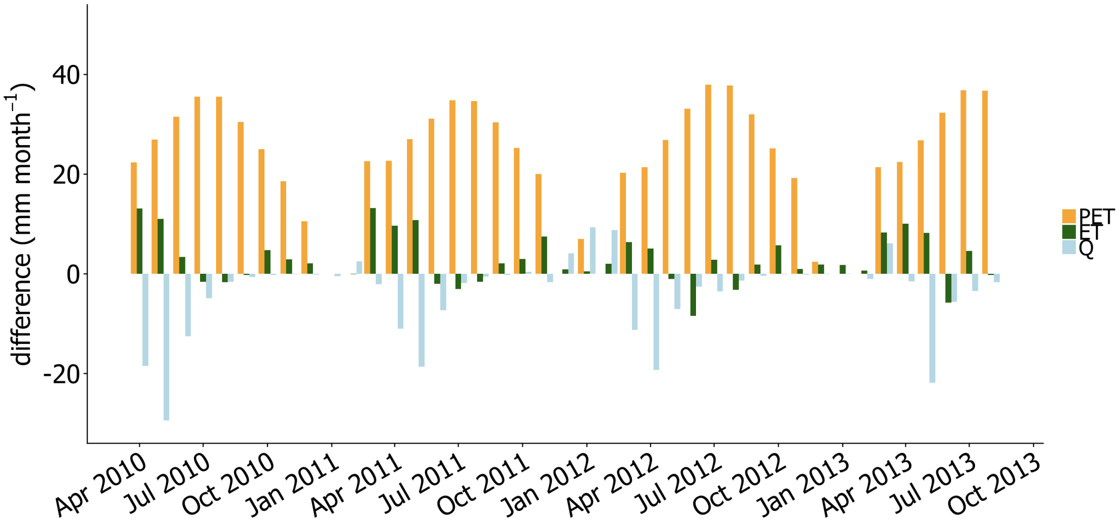

FIGURE 3.11: The differences in PET, ET and Q between control and warming simulations. By subtracting the PET, ET and Q values of the control simulation from the warming simulation, there is a continual increase in PET, general increase in ET and general decrease in Q. However, ET decreases in summer months and Q increases in winter and spring months. These trends coincide with differences in seasonal TWI, when rain and melt events are occurring more regularly during the winter in the warming simulation. The overall Q decrease is lessened by seasonal increases from high water supply (TWI) during a time of low water demand (PET).

I return to the Budyko framework to assess my annual and monthly results from Figure 3.11.The control simulation has an aridity index of 1.0, evaporative fraction 0.60 and runoff ratio of 0.36. The warming simulation has an aridity index of 1.4, evaporative fraction of 0.66 and runoff ratio of 0.28. Figure 3.12 shows that response in evaporative fraction due to a change in the aridity index from the control simulation to the warming simulation does not follow the slope of Budyko's expectation. The expectation is depicted as a hollow point in Figure 3.12. Instead, the evaporative fraction of the warming simulation falls below the expectation, increasing the anomaly from the Budyko curve. This evaporative fraction within the warming simulation reveals a reduced overall increase in ET and reduced overall decrease in Q, relative to the expected value based on the Budyko framework. As discussed in the next section, a reduced sensitivity results from a shift in TWI timing associated with warming.

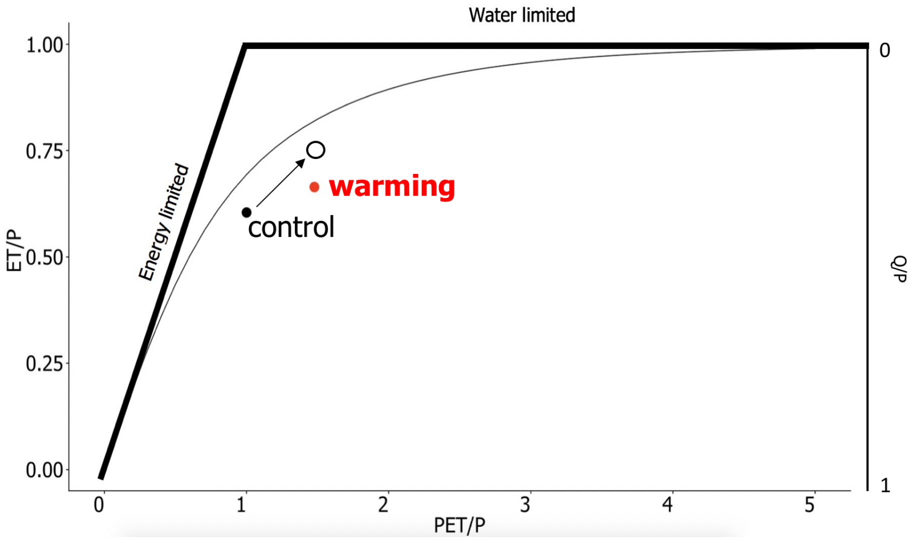

FIGURE 3.12: The evaporative fraction and aridity index of the control simulation (black), expected warming behavior (hollow) and warming (red) simulation. The hollow point represents an increase in ET due to PET, induced by a simulated warming, along the expected Budyko curve. The red point reveals a dampened increase in ET and, in turn, a reduced decrease in Q. The reduced movement of the warming simulation creates an anomaly from the Budyko curve. These reductions in hydrologic partitioning are associated with misalignment of water supply (TWI) and water demand (PET).

Chapter 4

Discussion

Overall, there is an increase in ET and a decrease in Q between the control and warming simulations within Gordon Gulch from April 2010 to October 2013. This reveals, holding all other environmental variables constant, an annual average streamflow decrease of 31mm, or 37% of total streamflow. This result is consistent with several previous studies: "business as usual" climate warming is predicted to decrease Q up to 17% by 2100 in the entire Colorado Basin [Christensen et al., 2004]. The entirety of western North America is predicted, by climate model ensembles and VIC, to decrease in runoff by 10-30% by 2050 [Milly et al., 2005; Christensen and Lettenmaier, 2007]. Conversely, global climate models have predicted a mean runoff increase of 2.9% per 1°C of warming [Zhang and Tang, 2014]. However, streamflow increases in the climate and earth system models at global [Zhang and Tang, 2014] and regional [McCabe and Wolock, 2016] scales incorporate additional independent variables, including changing precipitation and vegetation properties [Schilling et al., 2008]. Furthermore, these previous assessments of streamflow change under warming conditions do not additionally assess mechanisms for streamflow change.

Monthly analyses and isolation of climate warming effects isolate the mechanism for streamflow change in warming environments. Foster et al. [2016], separated mechanisms of increased ET and precipitation phase change and determined that increased ET decreases Q at a larger magnitude. Hamlet and Lettenmaier [1999] saw overall decreases in streamflow but with wintertime increases, consistent with our monthly analysis of streamflow change in Gordon Gulch. And Berghuijs et al. [2014] suggested that annual decreases in streamflow across hundreds of watersheds in the United States correspond to decreased snow fraction [Berghuijs et al., 2014]. Yet within snow-dominated catchments, there remains a need to decipher the quantitative effects of individual climate warming components. This is a particularly critical need within the upper montane zone, where there is a high sensitivity to hydrologic change induced by warming [Marks et al., 1998]. The upper montane zone remains vulnerable to small changes in energy creating large changes in annual hydrologic resources [Marks et al., 1998]. My analysis in Gordon Gulch, of the Colorado Rocky upper montane zone, isolates the mechanistic effects of warming and subsequent changes in precipitation phase to understand future changes in hydrologic partitioning under increased atmospheric demand (PET) and altered TWI seasonality (the timing of rainfall and snowmelt).

Monthly changes in PET, ET and Q, fluctuating in sign and magnitude over different seasons, and reduced vertical change along the Budyko curve suggest reduced sensitivity in ET and Q between the control and warming simulations relative to rain-dominated catchment. In the warming simulation, streamflow increases in winter and spring months, when the snow season has shortened, the snow fraction has decreased, and rainfall and melt events are occurring more frequently during these seasons. Instead of a large pulse of water input after the snowmelt season, direct precipitation and melt events spread the water input across a longer period of time. The original presence of snow in the control simulation allows for a change in precipitation phase, thereafter changing TWI timing, the timing of rain and snowmelt events. With climate warming, streamflow is sensitive to both increased PET and changing TWI timing, where increased PET acts to decrease Q but earlier TWI pulses acts to increase Q. Under warmer conditions, TWI increases in the winter when PET is low, decoupling water supply (TWI) and water demand (PET), and increasing winter and springtime runoff. Snowfall and the presence of a persistent snowpack buffers and offsets the overall decrease in Q due to simulated warming.

This outcome is echoed within the Budyko framework, where we see a smaller increase in ET due to a change in PET than expected along the Budyko curve. Instead of following the Budyko curve, represented by the hollow point in Figure 3.12, the warming simulation (red point) increases along the vertical axis at a reduced magnitude. This suggests that ET is less sensitive than expected to changes in PET. I associate the lower than expected increase in ET to a shift in the timing of TWI which acts to increase Q in winter and early spring, and decrease ET in summer months due to water limitation. This behavior occurs because TWI inputs, the catchment water supply, are shifted earlier in the spring when PET, the catchment water demand, is relatively low and hence the partitioning of TWI to Q during this time period is relatively high.

I determine that streamflow generation will decrease under simulated warming conditions, as a sum of the effects of increasing PET and changing TWI, consistent with previous studies focused on runoff and evapotranspiration sensitivity to climate warming [Foster et al., 2016; Berghuijs et al., 2014; Goulden and Bales, 2014]. I isolate the effects of changing TWI seasonality on streamflow generation through monthly ET and Q analysis and comparison within the Budyko framework, while holding all remaining environmental model variables constant. This simulated shift in TWI timing predicts significant changes in timing and amount of water resources within the upper montane zone: a result unique to snow-dominated systems and therefore with important implications for snow-dominated systems globally.

Chapter 5

Conclusion

Mountain snow is as an essential hydrologic resource for downstream communities globally. Within a warming simulation, the upper montane zone snow-fraction decreases, changing the hydrologic partitioning, rain events and snowmelt events, of the catchment. In Gordon Gulch, this means an annual decrease in streamflow of 37% with a seasonal 13% increase in streamflow during winter and spring months. I use DHSVM to simulate the sensitivity of evapotranspiration and streamflow under climate warming. Using the Budyko framework to reveal the effect of warming on hydrologic partitioning I show that reduced increases in ET and reduced decreases in Q are expected relative to rain-dominated systems. In this context, I show that hydrologic partitioning of Gordon Gulch is affected by increases in PET and changes in precipitation type and TWI associated with warming. Warming acts to both increase PET and ET and reduce the seasonality in TWI. Reduced TWI seasonality, in turn, acts to increase Q during winter and early spring. Hence, the presence of snow and associated changes in TWI offset the overall decrease in Q compared to a rain-dominated system, where TWI seasonality would not change with warming. This buffering effect has large implications for water resource management. Further modeling and observation-based studies are needed.

Bibliography

Alexander, R. R., Troendle, C. A., Kaufmann, M. R., Shepperd, W. D., Crouch, G. L., Watkins, R. K. (1985). The Fraser experimental forest, Colorado: Research program and published research 1937-1985. Gen. Tech. Rep. RM-118. 44 pp. Rocky Mt. For. And Range Exp. Stn., U.S. Dept. of Agric. For. Serve., Fort Collins, Colo.

Anderson, S. P., Anderson, R. S., Hinckley, E. L. S., Kelly, P., Blum, A. (2011). Exploring weathering and regolith transport controls on Critical Zone development with models and natural experiments. Applied Geochemistry, 26(SUPPL.), S3–S5. doi.org/10.1016/j.apgeochem.2011.03.014.

Anderson, S. P., Anderson, R. S., Tucker, G. ., Dethier, D. (2013). Critical zone evolution: Climate and exhumation in the Colorado Front Range, in Abbott, L.D., and Hancock, G.S., eds., Classic Concepts and New Directions: Exploring 125 Years of GSA Discoveries in the Rocky Mountain Region: Geological Society of America (Vol. 33). doi.org/10.1130/2013.0033(01).

Antonarakis, A. S., Saatchi, S. S., Chazdon, R. L., Moorcroft, P. R. (2011). Using Lidar and Radar measurements to constrain predictions of forest ecosystem structure and function. Ecological Applications. 21(4), 1120-1137. doi.org/10.1890/10-0274.1.

Bales, R. C., Molotch, N. P., Painter, T. H., Dettinger, M. D., Rice, R., Dozier, J. (2006). Mountain hydrology of the western United States. Water Resources Research, 42(8), 1–13. doi.org/10.1029/2005WR004387.

Barnett, T. P., Adam, J. C., Lettenmaier, D. P. (2005). Potential impacts of a warming climate on water availability in snow-dominated regions. Nature, 438(7066), 303–309. doi. org/10.1038/nature04141.

Barnhart, T. B., Molotch, N. P., Livneh, B., Harpold, A. A., Knowles, J. F., Schneider, D. (2016). Snowmelt rate dictates streamflow. Geophysical Research Letters, 43(15), 8006–8016.doi.org/10.1002/2016GL069690.

Beckers, J., Alila, Y. (2004). A model of rapid preferential hillslope runoff contributions to peak flow generation in a temperate rain forest watershed. Water Resources Research. 40(3). doi.org/10.1029/2003 WR002582.

Befus, Kevin Sheehan, A Leopold, Matthias Anderson, Suzanne Anderson, Robert. (2011). Seismic Constraints on Critical Zone Architecture, Boulder Creek Watershed, Front Range, Colorado. Vadose Zone Journal. 10. 915-927. 10.2136/vzj2010.0108.

Berghuijs, W. R., Woods, R. A., Hrachowitz, M. (2014). A precipitation shift from snow towards rain leads to a decrease in streamflow. Nature Climate Change, 4(7), 583–586. doi.org/10.1038/nclimate2246.

Bosson, E., Sabel, U., Gustafsson, L. G., Sassner, M., Destouni, G. (2012). Influences of shifts in climate, landscape, and permafrost on terrestrial hydrology. Journal of Geophysical Research Atmospheres, 117(5), 1–12. doi.org/10.1029/2011JD016429.

Brooks, E. S., Boll, J., Mcdaniel, P. A. (2004). A hillslope-scale experiment to measure lateral saturated hydraulic conductivity, 40, 1–10. doi.org/10.1029/2003WR002858.

Budyko, M. I.: Climate and Life, Academic Press, Orlando, FL, 508 pp., 1974.

Burns, M. A., Barnard, H. R., Gabor, R. S., McKnight, D. M, Brooks, P. D. (2016). Dissolved organic matter transport reflects hillslope to stream connectivity during snowmelt in a montane catchment. Water Resources Research. doi.org/ 10.1002/2015WR017878.

Cayan, D. R., Kammerdiener, S. A., Dettinger, M. D., Captrio, J.M, Peterson, D. H. (2001). Changes in the Onset of Spring in the Western United States. Bulletin of American Meteorological Society. doi.org/10.1175/15200477(2001)082<0399:CITOOS>2.3.CO;2.

Chauvin, G. M., Flerchinger, G. N., Link, T. E., Marks, D., Winstral, A. H., Seyfried, M. S. (2011). Long-term water balance and conceptual model of a semi-arid mountainous catchment. Journal of Hydrology, 400(1–2), 133–143. doi.org/10.1016/j.jhydrol.2011.01.031.

Chow, V.T. (1964). Handbook of Applied Hydrology. McGraw-Hill Book Company, USA.

Christensen, N. S., Lettenmaier, D. P. (2007). A multimodel ensemble approach to assessment of climate change impacts on the hydrology and water resources of the Colorado River Basin. Hydrology and Earth System Sciences Discussions, 11(4), 1417–1434.

Christensen, N. S., Wood, A. W., Voisin, N., Lettenmaier, D. P., Palmer, R. . (2004). The Effects of Climate Change on the Hydrology and Water Resources of the Colorado River Basin. Climate Change, 62, 337–363.

Christensen, N. S., Wood, A. W., Voisin, N., Lettenmaier, D. P., Palmer, R. N. (2004). The effects of climate change on the hydrology and water resources of the Colorado River basin. Climatic Change, 62(1–3), 337–363. doi.org/10.1023/B:CLIM.0000013684.136 21.1f.

Cowie, R. (2010). The Hydrology of Headwater Catchments from the Plains to the Continental Divide, Boulder Creek Watershed, Colorado. Thesis, University of Colorado, Master of Arts Department of Geography.

Cunderlick, M.J. (2003). Hydrologic model selection fort the CFCAS project: Assessment of water resources risk and vulnerability to changing climatic conditions, Project Report 1. University of Western Ontario, Canada.

Diek, S., Temme, A. J. A. ., Teuling, A. . (2014). The effect of spatial social variation on the hydrology of a semi-arid Rocky Mountains catchment. Geoderma, 113–126.

Du, E., Link, T. E., Gravelle, J. A., Hubbart, J. A. (2014). Validation and sensitivity test of the distributed hydrology soil-vegetation model (DHSVM) in a forested mountain watershed. Hydrological Processes, 28(26), 6196–6210. doi.org/10.1002/hyp.10110.

Frans, C., Istanbulluoglu, E., Mishra, V., Munoz-Arriola, F., Lettenmaier, D. P. (2013). Are Climatic or Land Cover Changes the Dominant Cause of Runoff Trends in the Upper Mississippi River Basin? Geophysical Research Letters. 40. 1104-1110. 10.1002/grl.50262.

Foster, L. M., Bearup, L. A., Molotch, N. P., Brooks, P. D., Maxwell, R. M. (2016). Energy budget increases reduce mean streamflow more than snow– rain transitions: using integrated modeling to isolate climate change impacts on Rocky Mountain hydrology. Environ. Res. Lett, 11. doi.org/10.1088/1748-9326/11/4/044015.

Gochis, D., et al. (2013). The Great Colorado Flood of September 2013. Bulletin of American Meteorological Society. doi.org/10.1175/BAMS-D-13-00241.1

Gordon Gulch, Boulder Critical Zone Observatory, (2011). criticalzone.org/boulder/infrastructure/field-area/gordon-gulch/.

Gosain, A.K., A. Mani and C. Dwivedi, 2009. Hydrologic Modelling-Literature Review. Climawater, Report NO.1.

Goulden, M. L., Bales, R. C. (2014). Mountain runoff vulnerability to increased evapotranspiration with vegetation expansion. Proceedings of the National Academy of Sciences, 111(39), 14071–14075. doi.org/10.1073/pnas.1319316111.

Gul, C., Muhammad, S., Ali, S. (2017). Using Landsat images to monitor changes in the snow- covered area of selected glaciers in northern Pakistan, 14, 2013–2027.

Gupta, V. K., Soroosh, S. (1998). Toward improved calibration of hydrological models: Multiple and noncommensurable measures of information. Water Resources Research, 34(4), 751–763.

Hall, D. K., Riggs, G. A., Salomonson, V. V. (1995). Development of methods for mapping global snow cover using moderate resolution imaging spectroradiometer data. Remote Sensing of the Environment. doi.org/10.1016/0034-4257(95)00137-P.

Hamlet, A. F., Lettenmaier, D. P. (1999). Effects of Climate Change on Hydrology and Water Resources in the Columbia River Basin. Journal of the American Water Resources Association. doi.org/10.1111/j.1752-1688.1999.tb04240.x.

Harpold, A. A., Molotch, N. P. (2015). Sensitivity of soil water availability to changing snowmelt timing in the western U.S. Geophysical Research Letters, 42(19), 8011–8020. doi.org/10.1002/2015GL065855.

Hinckley, E. ., Ebel, B. A., Barnes, R. T., Anderson, R. S., Williams, M. W., Anderson, S. P. (2012). Aspect control of water movement on hillslopes near the rain-snow transition of the Colorado Front Range. Hydrological Processes. doi.org/10.1002/hyp.9549.

Hongve, D. (1987). A revised procedure for discharge measurement by means of the salt dilution method. Hydrological Processes. 1(3), 267-260. doi.org/10.1002/hyp.3360010305.

Huang, X., Liang, T., Zhang, X., Guo, Z. (2011). Validation of MODIS snow cover products using Landsat and ground measurements during the 2001 – 2005 snow seasons over northern Xinjiang , China, 1161. doi.org/10.1080/01431160903439924.

Hunt, E. R. Jr., Running, S. W., Federer, C. A. (1991). Extrapolating plant water flow resistances and capacitances to regional scales. Agric For Meterol. 54, 169-195.

Jajarmizadeh, M., S. Harun and M. Salarpour, 2012. A Review on Theoretical Consideration of Models in Hydrology. Journal of Environmental Science and Technology.

Jennings, K., Winchell, T., Livneh, B., Molotch, N. P. (2018). Spatial variation of the rain-snow temperature threshold across the Northern Hemisphere. Nature Communications, 9(1148). doi.org/10.1038/s41467-018-03629-7.

Kaufman M. R., (1982). Leaf conductance as a function of photosynthetic photo flux density and absolute humidity different from leaf to air. Plant Physiol. 69, 1018-1022.

Kapnick, S. B., Yang, X., Vecchi, G. A., Delworth, T. L., Gudgel, R., Malyshev, S., Margulis, S. A. (2018). Potential for western US seasonal snowpack prediction. Proceedings of the National Academy of Sciences, 115(6), 201716760. doi.org/10.1073/pnas.17167 60115.

Kiang, J. E., Gazoorian, C., McMillan, H., Coxon, G., Le Coz, J., Westerberg, I. K., Mason, R. (2018). A Comparison of Methods for Streamflow Uncertainty Estimation. Water Resources Research. doi.org/10.1029/2018WR022708.

Kingston, D. G., Todd, M. C., Taylor, R. G., Thompson, J. R., Arnell, N. W. (2009). Uncertainty in the estimation of potential evapotranspiration under climate change. Geophysical Research Letters. 36(20). doi.org/10.1029/2009GL040267.

Kite, G. (1993). Computerized streamflow measurement using slug injection. Hydrological Processes. 7(2), 227-233. doi.org/10.1002/hyp.3360070212.

Klos, P. Z., Link, T. E., Abatzoglou, J. T. (2014). Extent of the rain-snow transition zone in the western U.S. under historic and projected climate. Geophysical Research Letters. doi.org/10.1002/2014GL060500.

Knowles, N., Park, M., Dettinger, M. D. (2005). Trends in Snowfall versus Rainfall in the Western United States Trends in Snowfall versus Rainfall in the Western United States, 1–32. doi.org/10.1175/JCLI3850.1.

Kormos, P. R., Marks, D., McNamara, J. P., Marshall, H. P., Winstral, A., Flores, A. N. (2014). Snow distribution, melt and surface water inputs to the soil in the mountain rain-snow transition zone. Journal of Hydrology, 519(PA), 190–204. doi.org/10.1016/j.jhydrol.2014.06.051.

Krause, P., Boyle, D. P., Bäse, F. (2005). Advances in Geosciences Comparison of different efficiency criteria for hydrological model assessment. Advances in Geosciences, 5(89), 89–97. doi.org/10.5194/adgeo-5-89-2005.

Kunkel, K. E., Palecki, M., Ensor, L., Hubbard, K. G., Robinson, D., Redmond, K., Easterling, D. (2009). Trends in twentieth-century U.S. snowfall using a quality-controlled dataset. Journal of Atmospheric and Oceanic Technology, 26(1), 33–44. doi.org/10.1175/2008JTECHA1138.1.

Kuzmin, V., Koren, V. (2008). Fast and efficient optimization of hydrologic model parameters using a priori estimates and stepwise line search, 109–128. doi.org/10.1016/j.jhydrol.2008.02.001.

Langston, A. L., Tucker, G. E., Anderson, R. S., Anderson, S. P. (2015). Evidence for climatic and hillslope-aspect controls on vadose zone hydrology and implications for saprolite weathering. Earth Surface Processes and Landforms, 40(9), 1254–1269.

Livneh, B., Deems, J. S., Buma, B., Barsugli, J. J., Schneider, D., Molotch, N. P., Wessman, C. A. (2015). Catchment response to bark beetle outbreak and dust-on-snow in the Colorado Rock Mountains. Journal of Hydrology, 196–210.

Luce, C. ., Abatzoglou, J. T., Holden, Z. A. (2013). The Missing Mountain Water:

Slower Westerlies Decrease Orographic Enhancement in the Pacific Northwest USA. Science, 342, 1360–1365. doi.org/10.1126/science.1242335.

Luce, C. H., Tarboton, D. G., Cooley, K. R. (1998). The influence of the spatial distribution of snow on basin-averaged snowmelt. Hydrological Processes, 12(10–11), 1671–1683. doi.org/10.1002/(SICI)1099-1085(199808/09)12:10/11<1671::AID-HYP688>3.0.CO;2-N.

Liu, C., K. Ikeda, G. Thompson, R. Rasmussen, (2011). High-Resolution Simulations of Wintertime Precipitation in the Colorado Headwaters Region: Sensitivity to Physics Parameterizations, Monthly Weather Review, doi: 10.1175/MWR-D-11-00009.1.

Manache, G. Melching, C.S. (2004). Sensitivity analysis of a water-quality model using Latin Hypercube Sampling. Journal of Water Resources Planning and Management, ASCE. 130 (3), 232-242.

Marks, D., Kimball, J., Tingey, D., Link, T. (1998). The sensitivity of snowmelt processes to climate conditions ans forest during rain on snow (SNOBAL).pdf. Hydrological Processes, 1587(March), 1569–1587.

McCabe, G. J., Wolock, D. M. (2016). Variability and Trends in Runoff Efficiency in the Conterminous United States. Journal of the American Water Resources Association, 52(5), 1046–1055. doi.org/10.1111/1752-1688.12431.

McKay, M. D., Beckman, R. J., W. J. Conover, W. J. (1979). Comparison of Three Methods for Selecting Values of Input Variables in the Analysis of Output from a Computer Code. Technometrics. 21:2, 239-245, DOI: 10.1080/00401706.1979.10489755.

Milly, P. C. D., Dunne, K. A., Vecchia, A. V. (2005). Global pattern of trends in streamflow and water availabilty in a changing climate. Nature. 438, 347-350. doi.org/10.1038/nature04312.

Milly, P. C. D., Dunne, K. A. (2016). Potential evapotranspiration and continental drying. Nature Climate Change, 6(10), 946–949. doi.org/10.1038/nclimate3046.

Mote, P. W., Li, S., Lettenmaier, D. P., Xiao, M., Engel, R. (2018). Dramatic declines in snowpack in the western US. Npj Climate and Atmospheric Science, 1(1), 2. doi.org/10.1038/s41612-018-0012-1.

Muleta, M. K., Nicklow, J.W. (2005). Sensitivity and uncertainty analysis coupled with automatic calibration for a distributed watershed model. Journal of Hydrology. 306(1-4), 127-145. doi.org/10.1016/j.jhydrol.2004.09.005.

Musselman, K. N., Clark, M. P., Liu, C., Ikeda, K., Rasmussen, R. (2017). Slower snowmelt in a warmer world. Nature Climate Change, 7(3), 214–219. doi.org/10.1038/nclimate3225. Natural Resources Conservation Service Soils (2018). nrcs.usda.gov/wps/portal/nrcs/site/co/.

Nash, J. E., Sutcliffe, J. V. (1970). River flow forecasting through conceptual models part I — A discussion of principles. Journal of Hydrology. 10(3), 282-290. doi.org/10.1016/0022-1694(70)90255-6.

Nayak, A., D. Marks, D. G. Chandler, and M. Seyfried (2010), Long-term snow, climate and streamflow trends from the Reynolds Creek Experimental Watershed, Owyhee Mountains, Idaho USA, Water Resour. Res., 46, W06519, doi:10.1029/2008WR007525.

Nijssen, B., O'Donnell, G. M., Lettenmaier, D. P., Lohmann, D., Wood, E. F. (2001). Predicting the discharge of global rivers. Journal of Climate, 14(15), 3307–3323. doi.org/ 10.1175/1520-0442(2001)014<3307:PTDOGR>2.0.CO;2.

Nowak, K. (2012). Colorado River Basin Hydroclimatic Variability. Journal of Climate. doi.org/10.1175/JCLI-D-11-00406.1. Pope, G., Treitz, P. (2013). Leaf Area Index (LAI) Estimation in Boreal Mixedwood Forest of Ontario, Canada Using Light Detection and Ranging (LiDAR) and WorldView-2 Imagery, (iii), 5040–5063. doi.org/10.3390/rs5105040.

Portmann, R. W., Solomon, S., Hegerl, G. C. (2009). Spatial and seasonal patterns in climate change, temperatures, and precipitation across the United States. Proceedings of the National Academy of Sciences, 106(18), 7324–7329. doi.org/10.1073/pnas. 0808533106.

Powers, J., Klemp, J., Skamarock W et al. (2017). The weather research and forecasting model: Overview, system efforts, and future directions. BAMS. doi.org/10. 1175/BAMS-D-15-00308.1.

PRISM (2018). http://prism.oregonstate.edu/.

Raleigh, M. S., Livneh, B., Lapo, K., Lundquist, J. . (2016). How does availability of meteorological forcing data impact physically-based snowpack simulations? Journal of Hydrometeorology, 17, 99–120. doi.org/10.1175/JHM-D-14-0235.1.

Rasmussen, R., Ikeda, K., Liu, C., Gochis, D., Clark, M., Dai, A., Zhang, G. (2014). Climate Change Impacts on the Water Balance of the Colorado Headwaters: High-Resolution Regional Climate Model Simulations. Journal of Hydrometeorology, 15(3), 1091–1116.

doi.org/10.1175/JHM-D-13-0118.1.

Regonda, S. K., Rajagopalan, B. (2004). Seasonal Cycle Shifts in Hydroclimatology over the Western United States. Journal of Climate. doi.org/10.1175/JCLI-3272.1. "Salt discharge measurement", Suzanne Anderson, (2016).

Scheff, J., Frierson, D. M. W. (2014). Scaling potential evapotranspiration with greenhouse warming. Journal of Climate, 27(4), 1539–1558. doi.org/10.1175/JCLI-D-13-00233.1.

Schilling, K. E., Jha, M. K., Zhang, Y., Gassman, P. W., Wolter, C. F. (2008). Impact of land use and land cover change on the water balance of a large agricultural watershed: Historical effects and future directions, 44, 1–12. doi.org/10.1029/2007WR006644.

Sharma, A. Tiwari, K. N. (2014). A comparative appraisal of hydrological behavior of SRTM DEM at catchment level. J. Hydrol. 519, 1394–1404.

Shaw, E.M., (1983). Hydrology in Practice. Chapman and Hall, London, UK. Pages: 569.

Song, X., Zhang, J., Zhan, C., Xuan, Y., Ye, M., Xu, C. (2015). Global sensitivity analysis in hydrological modeling: Review of concepts, methods, theoretical framework, and applications. Journal of Hydrology, 523, 739–757.

Stewart, J. R., Livneh, B., Kasprzyk, J. R., Rajagopalan, B., Minear, J. T., Raseman, W. J. (2017). A Multialgorithm Approach to Land Surface Modeling of Suspended Sediment in the Colorado Front Range. Journal of Advances in Modeling Earth Systems, 9(7), 2526–2544. doi.org/10.1002/2017MS001120.

Sturm, M., Taras, B., Liston, G. E., Derksen, C., Jonas, T., Lea, J. (2010). Estimating Snow Water Equivalent Using Snow Depth Data and Climate Classes. Journal of Hydrometeorology, 11(6), 1380–1394. doi.org/10.1175/2010JHM1202.1.

Surfleet, C. G., Iii, A. E. S., Mcdonnell, J. J. (2010). Uncertainty assessment of forest road modeling with the Distributed Hydrology Soil Vegetation Model (DHSVM), 1409, 1397–1409. doi.org/10.1139/X10-079.

Tang, Q., Lettenmaier, D. P. (2012). 21st century runoff sensitivities of major global river basins, 39(December 2011), 1–5. doi.org/10.1029/2011GL050834.

Thyer, M., Renard, B., Kavetski, D., Srikanthan, S. (2009). Critical evaluation of parameter consistency and predictive uncertainty in hydrological modeling: A case study using Bayesian total error analysis. Water Resources Research. 45(12), DOI: 10.1029/2008 WR006825.

USGS (2018). mrdata.usgs.gov/geology/state/state.php?state=CO.

van Griensven, A., Meixner, T., Grunwald, S., Bishop, T., Diluzio, M., Srinivasan, R. (2006). A global sensitivity analysis tool for the parameters of multi-variable catchment models. Journal of Hydrology. 324, 10-23. doi.org/10.1.1.464.2518.

van Wie, J. B., Adam, J. C., Ullman, J. L. (2013). Conservation tillage in dryland agriculture impcats watershed hydrology. Journal of Hydrology. 483, 26-38. doi.org/10.1016 /j.jhydrol.2012.12.030.

Vano, J., Nijssen, B., Lettenmaier, D.P. (2015). Seasonal hydrologic responses to climate change in the Pacific Northwest. Water Resources Research, 51, 1959–1976. doi.org

/10.1002/2014WR015909.

Walther, G. R., Post, E., Convey, P., Menzel, A., Parmesan, C., Beebee, T. J. C., Bairlein, F. (2002). Ecological responses to recent climate change. Nature, 416(6879), 389–395. doi.org/10.1038/416389a.

Westrick, K. J., Storck, P., Mass, C. (2002). Description and evaluation of a hydrometeorological forecast system for mountainous watersheds. Weather and Forecasting, 17, 250–262.

Wigmosta, M. S., and Burges, S. J. (1997). An adaptive modeling and monitoring approach to describe the hydrologic behavior of small catchments. Journal of Hydrology. 202, 48-77.

Wigmosta, M. S., Lettenmaier, D. (1999). A Comparison of Simplified Methods for Routing Topographically-Driven Subsurface Flow. Water Resources Research, 35, 255–264.

Wigmosta, M. S., Nijssen, B., Storck, P., Lettenmaier, D. (2002). The Distributed Hydrology Soil Vegetation Model, Mathematical Models of Small Watershed Hydrology and Applications. Water Resource Publications, 7–42.

Wigmosta, M. S., Perkins, W. (2001). Simulating the effects of forest roads on watershed hydrology, in Land Use and Watersheds: Human Influence on Hydrology and Geomorphology in Urban and Forest Areas. AGU Water Science and Application, 2, 127–143.

Wigmosta, M. S., Vail, L. W., Lettenmaier, D. P. (1994). A distributed hydrology-vegetation model for complex terrain. Water Resources, 30(6).

Williams, M. W., Seibold, C., Chowanski, K. (2009). Storage and Release of Solutes from a Subalpine Seasonal Snowpack: Soil and Stream Water Response, Niwot Ridge, Colorado. Biogeochemistry, 95(1), 77–94. doi.org/10.1007/s10533-009-9288-x.

Yao, C., Yang, Z. (2009). Parameters optimization on DHSVM model based on a genetic algorithm. Frontiers of Earth Science in China, 3, 364–380.

Zhang, Q., Knowles, J. F., Barnes, R. T., Cowie, R. M., Williams, M. W. (2018). Surface and subsurface water contributions to streamflow from a mesoscale watershed in complex mountain terrain, (February), 954–967. doi.org/10.1002/hyp.11469.

Zhang, X., Tang, Q. (2014). Runoff sensitivity to global mean temperature change in the CMIP5 Models. Geophysical Research . . . , 5492–5498. doi.org/10.1002/2014 GL060382.

Zhao, Q., Liu, Z., Ye, B., Qin, Y., Wei, Z., Fang, S. (2009). A snowmelt runoff forecasting model coupling WRF and DHSVM. Hydrology and Earth System Sciences, 13(10), 1897–1906. doi.org/10.5194/hess-13-1897-2009.